

Steric Effects in the Inelastic Scattering of NO(X) + Ar: Side-on Orientation

Victoria Walpole,^{†,§} Cornelia G. Heid,[†] Pablo G. Jambrina,^{*,‡} F. Javier Aoiz,^{*,¶}
and Mark Brouard^{*,†}

[†]*The Department of Chemistry, University of Oxford, Chemistry Research Laboratory, 12
Mansfield Rd, Oxford OX1 3TA*

[‡]*Departamento de Química Física, Universidad de Salamanca, 37008, Salamanca, Spain*

[¶]*Departamento de Química Física, Facultad de Química, Universidad Complutense, 28040
Madrid, Spain*

[§]*Current address: Max Planck Institute for Biophysical Chemistry, Am Faßberg 11, 37077
Göttingen, Germany*

E-mail: pjambrina@usal.es; aoiz@quim.ucm.es; mark.brouard@chem.ox.ac.uk

Abstract

The rotationally inelastic collisions of NO(X) with Ar, in which the NO bond-axis is oriented side-on (*i.e.* perpendicular) to the incoming collision partner, are investigated experimentally and theoretically. The NO(X) molecules are selected in the $|j = 0.5, \Omega = 0.5, \epsilon = -1, f\rangle$ state prior to bond-axis orientation in a static electric field. The scattered NO products are then state selectively detected using velocity-map ion imaging. The experimental bond-axis orientation resolved differential cross sections and integral steric asymmetries are compared with quantum mechanical calculations, and are shown to be in good agreement. The strength of the orientation field is shown to affect the structure observed in the differential cross sections, and to some extent

also the steric preference, depending on the ratio of the initial e and f Λ -doublets in the superposition determined by the orientation field. Classical and quantum calculations are compared and used to rationalise the structures observed in the differential cross sections. It is found that these structures are due to quantum mechanical interference effects, which differ for the two possible orientations of the NO molecule due to the anisotropy of the potential energy surface probed in the side-on orientation. Side-on collisions are shown to maximise and afford a high degree of control over the scattering intensity at small scattering angles ($\theta < 90^\circ$), whilst end-on collisions are predicted to dominate in the backward scattered region ($\theta > 90^\circ$).

1 Introduction

The initiation of any chemical reaction, and many molecular energy transfer processes, proceeds *via* molecular collisions. A detailed understanding of the forces that govern collisions between molecules and/or atoms is thus highly desirable and can provide important information regarding both the underlying energetic landscape as well as the preferred collision geometry. Stereospecificity is ubiquitous in nature, is important in atmospheric processes,^{1,2} and also plays a crucial role in industrial-scale catalytic procedures.³

In order to investigate the effects of the collision geometry on the scattering or reaction dynamics of a molecular system in the laboratory, a number of different methods have been used to align and orient molecules in space prior to collision. These include optical alignment methods,⁴⁻⁸ which employ laser polarisation to align the rotational angular momentum of a molecule, and electric⁹⁻¹³ or magnetic¹⁴⁻¹⁶ field orientation, which rely on the interaction of the field with polar and paramagnetic molecules and atoms, respectively.

Optical alignment has been applied, for instance, in a series of elegant experiments concerned with reactive collisions between CHD_3 and Cl ,⁴⁻⁶ where $\text{CHD}_3(v = 1, j = 1, \Omega = 0, \pm 1)$ was aligned with respect to the scattering frame (defined by \mathbf{k} and \mathbf{k}' , the initial and final relative velocity vectors). The studies reported pronounced differences in reactivity depending on the initial alignment of the CHD_3 molecules. Similarly, in a recent publication by Sharples *et al.*, the initial (\mathbf{j}) and final (\mathbf{j}') rotational angular momenta of electronically excited NO were selected and probed, respectively, using circularly polarised light to measure the rotational reorientation upon collision with neon atoms as a function of the scattering angle.⁷ Work by Perreault *et al.*^{8,17} used the Stark-induced adiabatic Raman passage (SARP) technique to align the angular momentum of HD molecules in collisions with unpolarised D_2 and H_2 molecules at cold collision energies (below 10 K). Their results show a three-fold stereodynamic preference for collisions of D_2 molecules with HD molecules that are aligned perpendicular to the relative velocity over HD molecules aligned parallel to \mathbf{k} .¹⁷

By means of optical methods, the molecular axis can only be *aligned* - either parallel or perpendicular to an axis of reference - even if circularly polarised light is used. However, using static electrical fields, molecules can be *oriented* such that the collision partner impacts at a specific end or side of the molecule. For example in the case of NO, the collision partner may collide at the N- or the O-end of the molecule. Previous work on NO plus rare gas collisions by Stolte and coworkers and our group has shown that, depending on the specific quantum state being probed, there is a pronounced preference for scattering off the N-end or the O-end of the molecule.^{11-13,18} Orientation of molecules can be achieved by the brute force method^{10,19} or by hexapole state selection coupled with adiabatic passage into a uniform electric^{9,11-13} or magnetic^{15,16} field. It has also been demonstrated that a magnetic guide is sufficient to orient paramagnetic atoms.²⁰

A slightly different way of controlling molecular collisions is to slow, or cool, down the collision partners. Stark decelerators have been used to slow down molecules and afford fine control of the collision energy.²¹⁻²³ Such low-energy collisions provide very high angular resolution, at which interesting quantum diffraction oscillations can be revealed. Using high-level *ab initio* calculations and the analytical Fraunhofer model, Onvlee *et al.* proposed that a prominent diffraction peak observed experimentally in the forward scattered region of the differential cross sections for collisions of NO with different rare gas atoms is dominated by the maximally possible m' value (within a given j' rotational level) and corresponds to a collision geometry in which the rare gas atom approaches the NO molecule from the side.²⁴ Although the orientation of the NO molecules was not actively controlled in these experiments, important steric information could be extracted from the quantum calculations. This particular study highlights the purely quantum nature of the scattering process at low temperatures.

In the ultracold regime ($T < 1 \mu\text{K}$), stereodynamic control has been realized in a quantum gas of KRb molecules.²⁵⁻²⁷ By confining molecules in an optical lattice and orienting their dipole moments along the confinement axis using electric fields, the molecules were forced to

orient with their dipole moments parallel to each other. By doing so, the reaction between molecules in the same quantum state could be largely suppressed due to the repulsive dipole-dipole interaction in the ‘side-by-side’ configuration.²⁷

In this article, we explore the role of molecular bond-axis orientation, specifically the side-on geometry, on the scattering dynamics of NO molecules colliding with Ar atoms. The NO molecules in our crossed molecular beam experiments are state selected in a hexapole and oriented in a static electric field prior to collision; the scattered, rotationally hot molecules are then state selectively detected by a resonance-enhanced multiphoton excitation (REMPI) scheme coupled with velocity-map ion imaging. Whilst a recent publication has focused on a subset of intermediate final rotational states corresponding to $\Delta j = 7$ to 12) and the most striking features,²⁸ here we present the full set of experimentally measured velocity-map ion images and extracted differential and integral cross sections from $\Delta j = 4$ to 15. We provide a more detailed account of the data analysis, including consideration of the detection efficiency. The x -axis integral steric effect, or integral steric asymmetry (ISA), is presented for the first time, and the influence of both attractive and repulsive interactions on the integral and differential steric effect is elucidated. The role of quantum interference is also discussed in detail, with consideration of a new treatment aimed at explaining the oscillatory behaviour of the ISA with Δj . Quasi-classical trajectory (QCT) calculations of the x -axis steric effect are also included for the first time, in order to establish the region in which the collision process becomes classical. By comparing our experimental data with fully quantum mechanical calculations for any arbitrary orientation of the NO molecule, we show that the preferred collision geometry in the forward scattered region ($\theta < 90^\circ$), and low to intermediate rotational excitations, is mostly side-on, whereas for larger scattering angles ($\theta > 90^\circ$), and higher rotational excitations, the end-on geometry dominates.

The paper is laid out as follows. The theory required to describe the bond-axis orientation resolved scattering of NO(X) with an atom is given in Section 2, followed in Section 3 by a discussion of the experimental and theoretical (both quasi-classical and quantum)

methods used. The data analysis method for extraction of the polarisation-dependent differential cross sections (r -PDDCSs) from the experimental ion images is given in Section 4. The experimental and computational differential and integral steric effects are presented in Sections 5.1 and 5.2, respectively, and are followed by a discussion of the dependence of the observed DCSs on the electric field strength, a comparison between quantum and classical regimes, and the mechanistic insights about the scattering process in Section 6. Finally, conclusions and the outlook for the future are given in Section 7.

2 Theory

2.1 Potential energy surfaces (PESs)

Nitric oxide (NO) is a $^2\Pi$ molecule with a single unpaired electron in an antibonding π^* orbital. In its electronic ground state, the rotational levels are split into two spin-orbit manifolds, defined by the magnitude of $|\Omega|$ ($= 0.5$ or 1.5), the projection of the rotational angular momentum (including electron spin), \mathbf{j} , onto the internuclear axis. The rotational levels in the two manifolds are separated by approximately 123 cm^{-1} . The rotational levels within each manifold are further split into two Λ -doublet states ($\epsilon = \pm 1, e/f$), which are almost degenerate, but differ in parity, $p = (-1)^{j-\epsilon/2} = \epsilon(-1)^{j-1/2}$.

Upon approach of a closed-shell atom toward NO(X), the interaction results in two potential energy surfaces (PESs) with different symmetries, A' and A'' , depending on the plane of approach relative to the occupied π^* orbital of the NO molecule. Inelastic scattering occurs simultaneously over both of these potentials, $V_{A'}$ and $V_{A''}$.²⁹ Under Hund's case (a), which holds for low and moderate rotational states, spin-orbit conserving ($\Delta\Omega = 0$) and changing ($\Delta\Omega = 1$) transitions may be considered to occur mainly on the half sum (V_{sum}) and half

difference (V_{dif}) potentials, respectively:³⁰

$$V_{\text{sum}}(\gamma, R) = \frac{1}{2} [V_{A''}(\gamma, R) + V_{A'}(\gamma, R)] = \sum_{\lambda=0}^{\lambda_{\text{max}}} V_{\lambda 0}(R) d_{00}^{\lambda}(\gamma) \quad (1)$$

$$V_{\text{dif}}(\gamma, R) = \frac{1}{2} [V_{A''}(\gamma, R) - V_{A'}(\gamma, R)] = \sum_{\lambda=2}^{\lambda_{\text{max}}} V_{\lambda 2}(R) d_{20}^{\lambda}(\gamma) \quad (2)$$

where $d_{mn}^{\lambda}(\gamma)$ are reduced Wigner rotation matrix elements, $V_{\lambda m}(R)$ are radially dependent expansion coefficients, \mathbf{R} is the distance between the atom and the center-of-mass of the diatom, and γ is the angle between \mathbf{R} and the internuclear axis, \mathbf{r} , of the diatom.

2.2 Electric-field orientation

The application of a static electric field to Λ -doublet selected molecules, under Hund's case (a), results in a wave function that may be described by a linear combination of the field free e and f states^{11,18,31,32}

$$|jm_E|\Omega|E\rangle = \frac{1}{\sqrt{2}} [\alpha(E) |jm_E|\Omega|e\rangle + \beta(E) |jm_E|\Omega|f\rangle] \quad (3)$$

where $|\Omega|$ is the absolute value of Ω , m_E is the projection of \mathbf{j} onto the electric field direction, E , and ϵ is the symmetry index. $\alpha(E)$ and $\beta(E)$ are field strength dependent mixing parameters,^{11,18,31,32}

$$|\alpha(E)| = \sqrt{1 - \frac{1}{\sqrt{1 + E_{\text{red}}^2}}} \quad \text{and} \quad |\beta(E)| = \sqrt{1 + \frac{1}{\sqrt{1 + E_{\text{red}}^2}}}, \quad (4)$$

where the strength of the reduced electric field is

$$E_{\text{red}} = \frac{2W_{\text{stark}}}{E_{\Lambda}}, \quad \text{and} \quad W_{\text{stark}} = -\epsilon \mu \mathbf{E} \frac{|\Omega m_E|}{j(j+1)} \quad (5)$$

describes the linear Stark effect. E_Λ is the Λ -doublet splitting and $\boldsymbol{\mu}$ is the static electric dipole moment of NO. At the experimental field strength (here 9.2 kV cm^{-1}) the mixing coefficients take values of $|\alpha| = 0.64$ and $|\beta| = 1.26$. In the limit of infinite field, $|\alpha| = |\beta| = 1$, whilst, when no field is applied, $|\alpha| = 0$ and $|\beta| = \sqrt{2}$, and the field free f Λ -doublet is recovered.^{12,13}

In the laboratory, described by the LAB frame where the static electric field is parallel to the Z -axis, as shown in Figure 1a, there is a distribution of bond-axis orientations. The probability of a specific orientation, described by the angle between \boldsymbol{E} and $\boldsymbol{\mu}$ (which is parallel to \boldsymbol{r}), within the distribution is determined by the magnitudes of the mixing parameters in eq 4,^{13,33,34}

$$P(\Theta_{\mu E}) = \frac{1}{2} [1 - |\alpha\beta| P_1(\cos \Theta_{\mu E})] . \quad (6)$$

The minus sign in the probability indicates that, in the case of the low-field seeking f Λ -doublet state, the N-end of the NO molecule points towards the negative electrode, and Ω and m_E have opposite signs (noting that \boldsymbol{E} also points towards the negative electrode, and is antiparallel to \boldsymbol{r}). The bond-axis distribution at the field strength of our experiments is indicated in blue in Figure 2. By switching the polarity of the electrodes, the orientation of the NO molecules can be inverted.

A full description of the formalism for bond-axis orientation in an arbitrarily directed electric field is given elsewhere both classically^{13,34–36} and quantum mechanically.²⁸ Here, for brevity, only the final results are shown. The bond orientation resolved differential cross sections (DCSs), for a specific direction of the electric field in the scattering frame (θ_E, ϕ_E) , as illustrated in Figure 1b, may be written in terms of the r -PDDCSs, the bond-axis (r) polarisation dependent differential cross sections,²⁸

$$\left[\frac{d\sigma}{d\omega}(\theta) \right]_{\theta_E}^{\phi_E} = \frac{\sigma_{\text{iso}}}{2\pi} \left\{ R_0^{(0)}(\theta) + 3A_0^{(1)} \left[R_0^{(1)}(\theta) P_1(\cos \theta_E) \right. \right. \\ \left. \left. + 2R_1^{(1)}(\theta) C_{11}(\theta_E, 0) \cos \phi_E \right] \right\} , \quad (7)$$

where σ_{iso} is the isotropic cross section in the presence of a field, $P_1(\cos\theta_E)$ is the first-order Legendre polynomial, and $C_{11}(\theta_E, 0) = -\sin\theta/\sqrt{2}$ is a modified spherical harmonic. The $A_0^{(1)}$ coefficient is the expectation value of the $P_1(\cos\Theta_{\mu E})$ term in eq 6, which takes a value of $-|\alpha\beta|/3$.^{28,33}

The r -PDDCSs in eq 7, $R_q^{(k)}(\theta)$, are the multipole moments of the collision probability distribution of internuclear axes. Classically, these may be written as:^{35,36}

$$R_q^{(k)}(\theta) = \int P(\theta, \theta_r, \phi_r) C_{kq}(\theta_r, \phi_r) d\omega_r = \langle C_{kq}(\theta_r, \phi_r) \rangle, \quad (8)$$

where $d\omega_r = d\cos\theta_r d\phi_r$ is the solid angle, and $P(\theta, \theta_r, \phi_r)$ is the probability distribution function written in terms of the expansion of modified spherical harmonics,

$$P(\theta, \theta_r, \phi_r) = \frac{1}{4\pi} \sum_k \sum_{q=-k}^{+k} (2k+1) R_q^{(k)}(\theta) C_{kq}^*(\theta_r, \phi_r). \quad (9)$$

By expressing eq 3 in terms of the field-free wave functions in the scattering frame, it is possible to write the quantum mechanical r -PDDCSs in terms of the scattering amplitudes,

$$f_{j'm'\Omega'\epsilon' \leftarrow jm\Omega\epsilon} \equiv F_{m'\epsilon'm\epsilon},^{28}$$

$$\frac{\sigma_{\text{iso}}}{2\pi} R_0^{(0)}(\theta) = [\alpha^2 Q_{1/2e, 1/2e} + \beta^2 Q_{1/2f, 1/2f}] \quad (10)$$

$$\frac{\sigma_{\text{iso}}}{2\pi} R_0^{(1)}(\theta) = Q_{1/2f, 1/2e} + Q_{1/2e, 1/2f} \quad (11)$$

$$\frac{\sigma_{\text{iso}}}{2\pi} R_1^{(1)}(\theta) = -\frac{1}{\sqrt{2}} [Q_{-1/2f, 1/2e} + Q_{1/2e, -1/2f}], \quad (12)$$

where the $Q_{m_1\epsilon_1, m_2\epsilon_2}$ are a shorthand notation to define the summation over the products of scattering amplitudes:

$$Q_{m_1\epsilon_1, m_2\epsilon_2} = \frac{1}{2k^2} \left[\sum_{m'} F_{m'\epsilon' m_1\epsilon_1} F_{m'\epsilon' m_2\epsilon_2}^* \right]. \quad (13)$$

Note here that the ‘isotropic’ moment, $R_0^{(0)}(\theta)$, which is proportional to the ‘isotropic’ DCS,

$$\left[\frac{d\sigma}{d\omega}(\theta) \right]_{\text{iso}} = \frac{\sigma_{\text{iso}}}{2\pi} R_0^{(0)}(\theta), \quad (14)$$

is field-strength dependent in the QM case, because the composition of the initial state depends on the field-strength through eq (3).

The current study explores collisions with side-on oriented NO molecules, which corresponds to orientation along the scattering frame x -axis. (In the scattering frame, the z -axis is parallel to \mathbf{k} , and the plane spanned by \mathbf{k} and \mathbf{k}' defines the $+xz$ hemiplane - see Figures 1 and 2.) The two side-on x -orientations are labelled according to the direction of the electric field vector, \mathbf{E} (defined from the positive to the negative electrode) in the scattering frame, as illustrated in Figure 2. For scattering in the $+x$ orientation (a), the direction of the electric field is given by $\theta_E = \pi/2$, $\phi_E = 0$, whereas in the $-x$ orientation (b), \mathbf{E} is given by $\theta_E = \pi/2$, $\phi_E = \pi$. Further, note that trajectories that lead to a specific outgoing \mathbf{k}' may occur over the near- or the far-side of the NO molecule. For example, in the $+x$ orientation, near-side scattering corresponds to repulsive scattering of the argon atom on the N-side, whereas far-side scattering corresponds to attractive scattering over the O-side, and *vice versa* for the $-x$ orientation. Unless otherwise stated, the $+x$ and $-x$ orientations will be considered to denote near-side scattering, which is dominant for all but the lowest Δj transitions, off the N-side and off the O-side, respectively.

End-on collisions, in which the rare gas atom impacts either at the N-end or the O-end of the molecule, correspond to orientation along the z -axis, in which case collisions are symmetric around \mathbf{k} , and θ_E is sufficient to specify the direction of the electric field (for O-end collisions, $\theta_E = 0$ ($+z$ orientation), for N-end collisions, $\theta_E = \pi$ ($-z$ orientation)).

3 Methods

3.1 Experimental methods

The crossed molecular beam apparatus used here has been described in great detail previously,^{13,37–39} consequently, only those aspects which are most pertinent to this study are discussed. A molecular beam composed of 10 % NO in Ar is produced using a pulsed General valve, at a backing pressure of 3 bar and a repetition rate of 10 Hz, and skimmed ($d = 3$ mm) before entering a hexapole state selector.^{40–43} Upon entrance to the hexapole field, the low-field seeking $|j = 0.5, |\Omega| = 0.5, \epsilon = -1, f\rangle$ state is focused into the interaction region, and the high field seeking $|j = 0.5, |\Omega| = 0.5, \epsilon = +1, e\rangle$ state expelled from the hexapole. At the center of the interaction region, the NO molecular beam is crossed (at right angles) by a beam of pure Ar formed by a pulsed Jordan valve, which is skimmed ($d = 3$ mm) at the entrance to the scattering chamber and operates at 5 Hz. Background subtraction was performed on a shot-by-shot basis.

To orient the NO bond-axis prior to the scattering event, the molecules in the scattering chamber are exposed to a static electric field (9.2 kV cm^{-1}) generated by a four-rod electrode assembly,^{13,34,44} arranged such that the field polarity (and consequently the bond-axis, \mathbf{r}) is perpendicular to the initial relative velocity, $\mathbf{k} = \mathbf{v}_{\text{Ar}} - \mathbf{v}_{\text{NO}}$. The field direction was switched every 200 shots in order to record both x -axis orientations, and to reduce experimental drift. A much more detailed description of this technique is given elsewhere.^{13,34,44}

The product NO molecules are then state-selectively ionised using $(1 + 1')$ REMPI; a probe laser (at approximately 226 nm) is tuned to the individual rotational line of the $\text{NO}(A \leftarrow X)$ transition, followed by ionisation using 308 nm light from a XeCl excimer laser. Velocity-map⁴⁵ ion imaging⁴⁶ is then used to extract ions onto a position sensitive detector, during which a static voltage of $\sim 1 \text{ kV}$ is applied to the orientation rods.^{13,34,44}

Data were recorded for the $|j', \Omega' = 0.5, \epsilon' = +1, e\rangle \leftarrow |j = 0.5, \Omega = 0.5, E\rangle$ (spin-orbit conserving) transitions, resulting from the scattering of $\text{NO}(X)$ with Ar at a (mean) collision

energy of 651 cm^{-1} . All data were recorded on the $Q_{21}+R_{11}$ (mixed) branch, with vertical (V) polarisation of the excitation laser, *i.e.* polarisation parallel to the time-of-flight axis, using a Rochon polariser. The treatment of the raw ion images to extract the relevant experimental r -PDDCSs and bond-orientation resolved DCSs is discussed in detail in Section 4.

3.2 Theoretical methods

3.2.1 Quantum-mechanical scattering calculations

Close-coupled (CC) quantum-mechanical (QM) calculations were performed on the V_{sum} and V_{dif} PESs of Alexander^{31,47} at the mean experimental collision energy ($E_{\text{coll}} = 651\text{ cm}^{-1}$), using the HIBRIDON⁴⁸ suite of codes. Rotational levels up to and including $j' = 20.5$, both Λ -doublet levels ($\epsilon = \pm 1$) and both spin-orbit manifolds ($\Omega = 0.5, 1.5$) were included in the scattering wave function. To ensure calculation convergence, the maximal partial wave was set to $J = 190.5$, corresponding to the classical impact parameter $b = 7.5\text{ Å}$. The r -PDDCSs are calculated from the relevant scattering amplitudes according to eqs 10–12, and the bond orientation resolved DCSs using eq 7, with $\theta_E = \pi/2$, $\phi_E = 0, \pi$ and the relevant values of $|\alpha|$ and $|\beta|$.

Experimentally, there is a distribution of collision energies; consequently, to allow comparison between QM calculations and experimental data, it is necessary to account for the collision energy spread. QM calculations were performed, as described above, over a range of collision energies between $E_{\text{coll}} = 530\text{ cm}^{-1}$ and $E_{\text{coll}} = 740\text{ cm}^{-1}$ with a spacing of 30 cm^{-1} , these were then weighted to a Gaussian energy distribution with a FWHM of 35 cm^{-1} and a mean value of $E_{\text{coll}} = 651\text{ cm}^{-1}$.

3.2.2 Quasi-classical trajectory calculations

The quasi-classical trajectory (QCT) method used here is detailed fully elsewhere,^{35,49} and only specific aspects which are relevant to this work are mentioned here. Calculations were run using approximately 2×10^7 trajectories on the V_{sum} potential described above.

The length of the NO bond was fixed at its equilibrium length throughout the calculation using Lagrangian multipliers.⁴⁹ Since classically the rotational angular momentum may vary continuously, it is necessary to quantise the final angular momentum quantum number ($|j'| = \hbar\sqrt{j'(j'+1)}$); the real final j' values were rounded to the nearest integer to allow comparison with QM calculations. The maximum impact parameter, $b_{\text{max}} = 8.0 \text{ \AA}$, was determined such that beyond this value, no inelastic trajectories were observed. The r -PDDCs were calculated according to eq 8, and the bond orientation resolved DCSs from eq 7, analogously to the QM calculation, with $\theta_E = \pi/2$, $\phi_E = 0, \pi$ and the relevant values of $|\alpha|$ and $|\beta|$.

4 Data Analysis

The data analysis method used to fit the experimental ion images for unoriented scattering have been discussed in detail previously.^{37,38,50,51} It is necessary to extend this method to account for orientation of the NO bond-axis prior to the scattering event. Whilst the discussion here focuses on orientation with respect to the x -axis, the method applies to any arbitrary orientation of the bond-axis, including orientation with respect to the z -axis (end-on collisions).

4.1 Conversion from the time-of-flight to the scattering frame

The bond-axis resolved DCSs in eq 7 are written in terms of the extrinsic and intrinsic distributions of the NO bond-axis, in which the direction of the electric field is expressed in the scattering (xyz) frame (Figure 1b). In order to analyse the experimental ion images it is necessary to define the direction of the electric field with respect to the experimental geometry in which both the direction of the field, \mathbf{E} , and time-of-flight (TOF) direction are defined. The TOF frame ($X_T Y_T Z_T$), shown in Figure 1c, is defined such that Z_T is parallel to the TOF direction (which is perpendicular to the plane of the molecular beams), X_T is

parallel to \mathbf{k} (and consequently parallel to the scattering frame z -axis), and Y_T is defined such that the frame is right handed. In this frame, the direction of the electric field relative to the TOF axis is described by the angles (Θ_E, Φ_E) , and ϕ_T is the dihedral angle between the $X_T Z_T$ plane and the $\mathbf{k}\mathbf{k}'$ -plane (and the azimuthal angle between the xz -plane and the TOF axis in the scattering frame).

Rotation between the TOF and scattering frames may be achieved using a Wigner rotation matrix with elements $D_{q'q}^k(\alpha, \beta, \gamma)$. Following the convention of Zare,⁵² the conversion from the space-fixed ($X_T Y_T Z_T$) to the molecule-fixed (xyz) frame results from three successive rotations

1. A counter-clockwise rotation of angle α about the Z_T -axis.
2. A counter-clockwise rotation of angle β about the Y'_T -axis.
3. A counter-clockwise rotation of angle γ about the z -axis.

The Y'_T -axis refers to the position of the original Y_T -axis after the first rotation, and analogously for the other axes. The relative orientations of the TOF axis, \mathbf{k} , and \mathbf{k}' are fixed, consequently they remain stationary during the transformation. From this information it can be shown that the angles of rotation are necessarily $(\alpha, \beta, \gamma) = (\pi, -\pi/2, -\phi_T)$; note that if \mathbf{k}' lies in the plane of the molecular beams (*i.e.* perpendicular to the TOF axis), then $\phi_T = \pi/2$ in the $+Y_T$ hemisphere and $-\pi/2$ in the $-Y_T$ hemisphere.

To write eq 7 in terms of the TOF frame quantities, the Legendre polynomial in the second term and the expression $C_{11}(\theta_E, 0) \cos \phi_E$ in the third term, can be rewritten using only modified spherical harmonics functions, $C_{1q}(\theta_E, \phi_E)$:

$$P_1(\cos \theta_E) = C_{10}(\theta_E, \phi_E) , \quad (15)$$

and

$$C_{11}(\theta_E, 0) \cos \phi_E = \frac{1}{2} [C_{11}(\theta_E, \phi_E) - C_{1-1}(\theta_E, \phi_E)] . \quad (16)$$

Using the Euler angles for the rotation described above, the expressions in eqs 15 and 16 may then be written in terms of the TOF frame angles,

$$C_{1q}(\theta_E, \phi_E) = \sum_{q'} D_{q'q}^1(\pi, -\pi/2, -\phi_T) C_{1q'}(\Theta_E, \Phi_E) , \quad (17)$$

where $D_{q'q}^1(\pi, -\pi/2, -\phi_T)$ is the Wigner rotation matrix describing the rotation between frames. Applying this transformation to eq 15 results in

$$\begin{aligned} C_{10}(\theta_E, \phi_E) &= \frac{1}{\sqrt{2}} [C_{1-1}(\Theta_E, \Phi_E) - C_{11}(\Theta_E, \Phi_E)] \\ &= \sin \Theta_E \cos \Phi_E . \end{aligned} \quad (18)$$

The corresponding process for the $k = 1, q = \pm 1$ case in eq 16 requires use of the relation

$$C_{1\pm 1}(\theta_E, \phi_E) = \frac{e^{\pm i\phi_T}}{\sqrt{2}} [i \sin \Theta_E \sin \Phi_E \mp \cos \Theta_E] , \quad (19)$$

which gives

$$C_{11}(\theta_E, 0) \cos \phi_E = -\frac{1}{\sqrt{2}} [\sin \phi_T \sin \Theta_E \sin \Phi_E + \cos \phi_T \cos \Theta_E] . \quad (20)$$

Eq 7 may then be rewritten in terms of the TOF frame angles

$$\begin{aligned} \left[\frac{d\sigma}{d\omega}(\theta) \right]_{\theta_E}^{\phi_E} &= \frac{\sigma_{\text{iso}}}{2\pi} \left\{ R_0^{(0)}(\theta) + 3A_0^{(1)} \left[R_0^{(1)}(\theta) \sin \Theta_E \cos \Phi_E \right. \right. \\ &\quad \left. \left. - \sqrt{2} R_1^{(1)}(\theta) (\sin \phi_T \sin \Theta_E \sin \Phi_E + \cos \phi_T \cos \Theta_E) \right] \right\} . \end{aligned} \quad (21)$$

For orientation along the scattering frame x -axis, $\Theta_E = \pi/2$ and $\Phi_E = \pi/2$ or $3\pi/2$; consequently, the second and last terms in eq 21 goes to zero, and the DCS may be simplified to

$$\left[\frac{d\sigma}{d\omega}(\theta) \right]_{\theta_E=\pi/2}^{\phi_E=\pi/2, 3\pi/2} = \frac{\sigma_{\text{iso}}}{2\pi} \left\{ R_0^{(0)}(\theta) \mp 3\sqrt{2} A_0^{(1)} R_1^{(1)}(\theta) \sin \phi_T \right\} , \quad (22)$$

which depends on the angle ϕ_T . Thus, the oriented DCS depends on the elevation of the scattering products out of the plane of the molecular beams, and is not (unlike for orientation along the z -axis) symmetrically distributed about \mathbf{k} . For orientation along the z -axis (end-on orientation, with $\Theta_E = \pi/2$ and $\Phi_E = 0$ or π), the second term in eq 21 containing the $R_0^{(1)}(\theta)$ moment is retained, while the third term disappears and the scattering distributions for either end are independent of ϕ_T .

If the electric field is oriented along the y -axis and scattering occurs in the plane of the molecular beams, *i.e.* $\Theta_E = 0$ or π and $\phi_T = \pi/2$, eq 21 is further reduced to the ‘isotropic’ DCS, as defined in eq 14, and the two orientations have the same DCS. (Note that the same result is obtained directly in the scattering frame when the field is oriented along the scattering frame y -axis ($\theta_E = \pi/2$ and $\phi_E = \pi/2, 3\pi/2$) reducing eq 7 to eq 14.) It can also be shown that the isotropic DCS in eq 14 is equal to the half sum of the DCSs for the two x -axis, or the two z -axis, orientations, *i.e.*,

$$\left[\frac{d\sigma}{d\omega}(\theta) \right]_{\text{iso}} = \frac{1}{2} \left[\frac{d\sigma}{d\omega}(\theta) \right]_{+x} + \frac{1}{2} \left[\frac{d\sigma}{d\omega}(\theta) \right]_{-x} \quad (23)$$

$$= \frac{1}{2} \left[\frac{d\sigma}{d\omega}(\theta) \right]_{+z} + \frac{1}{2} \left[\frac{d\sigma}{d\omega}(\theta) \right]_{-z} . \quad (24)$$

4.2 Detection Efficiency

As indicated in Figure 2, each of the two experimental configurations includes both the $+x$ and the $-x$ geometry depending on whether \mathbf{k}' lies in the same or opposite hemisphere as the electric field vector. A consequence of this is that each image contains the scattering distributions of both the $+x$ and the $-x$ orientation (on either side of \mathbf{k}). If the detection efficiency were homogeneous across the image, then one image would in fact be sufficient to extract all the scattering information for both sides. However, due to different LAB frame velocities, molecules detected in the lower left portion of the images (close to where the lab velocity is zero) move slowly and therefore have a higher detection probability than molecules

with a higher LAB frame velocity in the upper right portion of the images. We refer to the portion to the left of \mathbf{k} as the ‘slow’ side, and the portion to the right of \mathbf{k} as the ‘fast’ side of the image. Due to the fast side of the image having significantly lower signal levels, extraction of the DCSs from this side has a much larger uncertainty compared to the slow side. By collecting images in both configurations and analysing the data in terms of the sum and difference images, as explained below, both halves of each image are included in the analysis.

4.3 Method of data fitting

In much the same way as for extraction of experimental DCSs^{50,51,53} and j' -PDDCSs,³⁷ the experimental r -PDDCSs (and consequently the bond orientation resolved DCSs) may be obtained using a Fourier moment fitting method.⁵⁴ Having established the relation between the out-of-plane scattering angle, ϕ_T , and the bond orientation resolved DCS, it is possible to relate the sum and difference of the $\pm x$ -orientations according to

$$\begin{aligned} \left[\frac{d\sigma}{d\omega}(\theta) \right]_{\text{sum}} &= \left[\frac{d\sigma}{d\omega}(\theta) \right]_{\pi/2}^0 + \left[\frac{d\sigma}{d\omega}(\theta) \right]_{\pi/2}^{\pi} \\ &= 2 \frac{\sigma_{\text{iso}}}{2\pi} R_0^{(0)}(\theta) , \end{aligned} \quad (25)$$

and

$$\begin{aligned} \left[\frac{d\sigma}{d\omega}(\theta) \right]_{\text{dif}} &= \left[\frac{d\sigma}{d\omega}(\theta) \right]_{\pi/2}^0 - \left[\frac{d\sigma}{d\omega}(\theta) \right]_{\pi/2}^{\pi} \\ &= 2\sqrt{2} |\alpha\beta| \frac{\sigma_{\text{iso}}}{2\pi} R_1^{(1)}(\theta) \sin \phi_T . \end{aligned} \quad (26)$$

This conveniently separates the contributions from the two relevant bond orientation moments, allowing independent fits to the sum and difference of the experimental ion images.

The intensities of the sum and difference images at a pixel coordinate (x, y) , for a single

scattering event, are proportional to eqs 25 and 26, and may be written

$$i_{\text{sum}}(x_n, y_n, j_n, j'_n, j_n^*, \Gamma_n) = 2z(x_n, y_n, j_n, j'_n) R_0^{(0)}(\theta_n) A(x_n, y_n, j'_n, j_n^*, \Gamma_n) , \quad (27)$$

for the summed image and,

$$i_{\text{dif}}(x_n, y_n, j_n, j'_n, j_n^*, \Gamma_n) = 2\sqrt{2} |\alpha\beta| z(x_n, y_n, j_n, j'_n) R_1^{(1)}(\theta_n) \sin(\phi_T)_n \\ \times A(x_n, y_n, j'_n, j_n^*, \Gamma_n) , \quad (28)$$

for the difference image. Eqs 27 and 28 are each composed of three terms; the polarisation information (which depends on the polarisation of the excitation laser), $A(x_n, y_n, j'_n, j_n^*, \Gamma_n)$, the variation in detection probability due to experimental parameters, $z(x_n, y_n, j_n, j'_n)$, and the angular scattering probability (related to the r -PDDCSs, $R_q^{(k)}(\theta)$). j_n and j'_n are the initial and final rotational angular momenta of the NO molecule, j_n^* is the rotational level the NO molecule is excited to in the A state, and Γ_n specifies the relative orientation of the laser propagation vectors and the scattering frame.^{37,50}

The $A(x_n, y_n, j'_n, j_n^*, \Gamma_n)$ (polarisation) term in eqs 27 and 28 accounts for the detection efficiency for different polarisations of the excitation laser. Whilst much of the literature uses the full QM j' -PDDCSs to this end,^{13,34,37,39,55} a full description of the bond-axis orientation resolved j' -PDDCSs is not currently available. However, it has been shown that the kinematic apse model, in which the projection of \mathbf{j} onto the kinematic apse is conserved throughout the scattering process, is a relatively good approximation of the QM collision induced alignment (*i.e.* for linearly polarised light) in unoriented scattering.^{38,43,50,53,56} It is expected that the polarisation correction will not strongly depend on the initial bond-axis orientation, due to the largely classical nature of the collision induced alignment for the scattering of NO(X) with Ar.^{38,56} Test calculations for end-on scattering (*i.e.* orientation with respect to the z -axis), for which bond orientation resolved j' -PDDCSs may be calculated due to the symmetry about \mathbf{k} , have shown that the bond orientation resolved alignment moments of the QM j' -

PDDCSs do not deviate far from the unoriented case. It is expected that this will also be true for orientation with respect to the x -axis.

The $R_q^{(k)}(\theta)$ moments in eq 27 and 28 may both be expanded in terms of modified spherical harmonics,

$$R_0^{(0)}(\theta) = \sum_l \frac{2l+1}{2} a_l C_{l0}(\theta, 0) \quad (29)$$

$$R_1^{(1)}(\theta) = \sum_l \frac{2l+1}{2} a_l C_{l1}(\theta, 0) , \quad (30)$$

where a_l are the expansion coefficients. The intensity at each pixel in eqs 27 and 28 may therefore be written as a linear combination of basis functions according to

$$i(x_n, y_n, j_n, j'_n, j_n^*, \Gamma_n) = \sum_l \frac{2l+1}{2} a_l b_l(x_n, y_n, j_n, j'_n, j_n^*, \Gamma_n) , \quad (31)$$

with the basis functions

$$b_l(x_n, y_n, j_n, j'_n, j_n^*, \Gamma_n) = 2C_{l0}(\theta, 0) z(x_n, y_n, j_n, j'_n) A(x_n, y_n, j'_n, j_n^*, \Gamma_n) \quad (32)$$

and

$$\begin{aligned} b_l(x_n, y_n, j_n, j'_n, \Gamma_n) &= 2\sqrt{2} |\alpha\beta| C_{l1}(\theta, 0) z(x_n, y_n, j_n, j'_n) \sin(\phi_T)_n \\ &\times A(x_n, y_n, j'_n, j_n^*, \Gamma_n) , \end{aligned} \quad (33)$$

for the sum and difference images, respectively. The total intensity of the image may then be written as:

$$I(x, y,)_{\text{sum/dif}} \approx \sum_n i_{\text{sum/dif}}(x_n, y_n, j_n, j'_n, j_n^*, \Gamma_n) = \sum_l \frac{2l+1}{2} a_l B_l(x_n, y_n, j_n, j'_n, j_n^*, \Gamma_n) , \quad (34)$$

where the basis function is

$$B_l(x_n, y_n, j_n, j'_n, j_n^*, \Gamma_n) \approx \sum_n b_l(x_n, y_n, j_n, j'_n, j_n^*, \Gamma_n) . \quad (35)$$

The basis sets are calculated using a Monte Carlo simulation, which has been discussed elsewhere,^{38,50,53} using of the order of 1×10^7 trajectories.

The basis sets described above were then used to fit the experimental images in Fourier space using a genetic algorithm, which is described elsewhere.^{37,38,50} The $\pm x$ DCSs were retrieved by substituting the experimentally determined $R_q^{(k)}(\theta)$ moments into eq 22 using the relevant values of $\Phi_E = \pi/2$ or $3\pi/2$, and $\phi_T = \pi/2$. The relative intensity of the sum and difference images is conserved during the analysis process, however, to compare the results to the QM r -PDDCSs and DCSs it is necessary to scale the experimental data; this is done with a single factor. Errors are calculated as the standard deviation of the fits to the slow and fast sides of the image and the total image.

The integral steric asymmetry, which has been previously defined for orientation with respect to the z -axis,^{12,13,32,44,57} may be defined for orientation with respect to the x -axis according to

$$S_x = \frac{\sigma_{+x} - \sigma_{-x}}{\sigma_{+x} + \sigma_{-x}} , \quad (36)$$

where $\sigma_{\pm x}$ are the $\pm x$ oriented integral cross sections. The steric asymmetry in eq 36 may be related to the integral bond orientation polarisation parameters, according to

$$\frac{r_1^{(1)}}{r_0^{(0)}} = \frac{S_x}{\sqrt{2} |\alpha\beta|} , \quad (37)$$

where the integral bond orientation moments are

$$r_q^{(k)} = \int_{-1}^{+1} R_q^{(k)}(\theta) \, d \cos \theta . \quad (38)$$

Note that the latter integral is only over $\cos \theta$ and not over the azimuthal angle.

5 Results

5.1 Differential steric effects

5.1.1 Experimental ion images

As already mentioned, each experimental ion image contains both the $+x$ and the $-x$ orientation data. This is illustrated in the two images in the top left of Figure 3. The ‘ $+x$ ion image’ has the electric field pointing from bottom left to top right; for scattering of the NO molecule into the bottom left of the image (corresponding to $\mathbf{k}' = \mathbf{v}'_{\text{Ar}} - \mathbf{v}'_{\text{NO}}$ pointing towards the top right of the image), the x -axis also points from bottom left to top right (*i.e.* parallel to \mathbf{E}), and the orientation is $+x$. Meanwhile, for NO scattering into the top right of the image, the x -axis points from top right to bottom left and is anti-parallel to \mathbf{E} , consequently the orientation in this portion of the image is $-x$. The same type of analysis for the ‘ $-x$ ion image’ (in which \mathbf{E} points from top right to bottom left) results in the bottom and top portions of the image having orientations of $-x$ and $+x$, respectively. The experimental images presented in the following are labelled according to the configuration corresponding to the more intense slow side.

Figure 3 shows experimental and (QM) simulated bond orientation resolved ion images for the spin-orbit conserving collisions of NO with Ar into the final e Λ -doublet for the j' states between $4.5e$ and $15.5e$. The colour scale for a specific $\Delta j = j' - j$ is equivalent in the $+x$ (column 1) and $-x$ (column 2) images, so as to retain the relative intensity information (*i.e.* that arising from the integral steric effect). The figure shows the experimental and simulated sum images in columns 3 and 4, and the experimental and simulated difference images in columns 5 and 6, respectively. The difference images were obtained by subtracting the $-x$ image from the $+x$ images, as described in Section 4.3.

The agreement between the experimental data and the QM simulations is generally excellent, for both the sum and the difference images. Several trends are observed, some of which have also been seen in the unoriented case^{38,39,43,51,53} and for orientation with respect to the

z -axis.^{13,34} Firstly, as j' increases, the scattering, which is very forwards for low rotational states, becomes progressively more sideways and then more backwards scattered. This arises as more ‘head-on’ collisions are required to access higher rotational states, which result in more backwards scattered angular distributions than ‘glancing blow’ collisions which involve a much smaller rotational energy transfer. Secondly, the ion images become smaller with increasing final rotational state, as more of the incoming translational energy is converted to rotational energy, resulting in lower outgoing translational energy and ion images with smaller radii. Thirdly, there is a pronounced alternation in the overall signal intensity (*i.e.* the overall scattering cross section) in the $+x$ and the $-x$ images as a function of j' . This trend is particularly obvious in the difference images where yellow/red corresponds to positive, black to zero, and blue/purple to negative intensities. For odd Δj transitions, the intensity on the slow side of the image (bottom left) is predominantly positive and indicates a preference for the $+x$ orientation, while for even Δj transitions, the intensity on the slow side is predominantly negative, indicating a preference for the $-x$ orientation (and *vice versa* on the fast side (top right) of the image). The node observed along \mathbf{k} marks the transition between the $+x$ hemisphere and the $-x$ hemisphere in the scattering frame. In addition to the trends related to the integral intensity of the images, differences between the scattering distributions for the two sides are also apparent: multiple peaks are observed in the $+x$ -orientation for odd intermediate Δj ($\Delta j = 7 - 13$), but only single peaks for even Δj ; and a single peak is observed for all states in the $-x$ -orientation. For all rotational states, the $+x$ -orientation is typically more forwards scattered than the $-x$ -orientation.

5.1.2 Orientation resolved differential cross sections

The experimental bond orientation resolved DCSs extracted from the ion images in Figure 3 are shown in Figure 4, alongside the QM DCSs (which have been averaged over the experimental energy distribution as described in Section 3.2.1). The grey shading shows the (field dependent) isotropic DCS, which is directly proportional to $R_0^{(0)}(\theta)$, see eq 14. In general,

the agreement between the QM and experimental data is good, and the majority of the calculated features are observed experimentally. Note the shape of the experimental data in the forwards scattered region of the $-x$ -orientation for $j' = 5.5e, 7.5e$ and $9.5e$; whilst the magnitude of the experimental DCS increases for low angle scattering, the peak shape observed in the QM DCS is not that well reproduced. This is likely due to the limited resolution in the experiment ($15 - 20^\circ$). The relatively poor agreement for $\Delta j = 9$ and 10 is due to the overlap of intensity in the ion image with the position at which the LAB frame velocity is zero. Any small errors in the laboratory detection efficiency factor, $z(x_n, y_n, j_n, j'_n)$ in eqs 27 and 28, leads to a poor representation of the detection efficiency in this region, and consequently a poorer fit.

As observed in the experimental ion images in Figure 3, the extracted experimental DCSs become more backwards scattered with increasing Δj , as more head-on collisions are required to access states with larger final rotational angular momentum. The alternation of the preference for $+x$ (odd Δj) and $-x$ (even Δj) scattering, observed in the ion images is also observed in the DCSs. The isotropic (field dependent) DCSs lie between the $\pm x$ -orientations resolved DCSs; this is to be expected since the bond orientation resolved DCSs are essentially deviations from the $R_0^{(0)}(\theta)$ moment.

As already seen in the experimental ion images, a double peak is apparent in the $+x$ DCS for odd Δj (particularly for $\Delta j = 7, 9, 11, 13$), while only a single peak is observed in the $+x$ DCS for even Δj and for the $-x$ orientation for both odd and even Δj . This propensity is observed for all except the very highest Δj transitions. For states with odd Δj , the experimental data show a strong preference for forwards scattering ($\theta < 90^\circ$) in the $+x$ -orientation which is almost completely suppressed in the $-x$ -orientation; this is in good agreement with the QM calculations and shows that the steric effect is very strong for $\theta < 90^\circ$.

5.1.3 Bond orientation moments

The $R_0^{(0)}(\theta)$ and $R_1^{(1)}(\theta)$ moments, defined in eq 10 and 12, respectively, quantify the isotropic and the orientation-dependent contributions to the scattering dynamics. As detailed in Section 4, it is these moments which we extract from the experimental sum and difference images, and from which we subsequently calculate the DCSs (eq 22). Consequently, any errors in the experimental r -PDDCSs will be manifested in the DCSs shown in Figure 4.

The experimental and QM r -PDDCSs are presented in Figure 5. The agreement is generally good; those states which were noted to have less good agreement of their bond orientation resolved DCSs (in Figure 4) with theory also have less good agreement of their r -PDDCSs. In particular, the second peak observed in the QM $R_0^{(0)}(\theta)$ moment is observed only as a shoulder on the more forwards scattered peak for $\Delta j = 7$ and 9; as mentioned above, this is likely due to small errors in the laboratory detection efficiency factor as well as the experimental resolution.

While the $R_0^{(0)}(\theta)$ moment depends directly on a mixture of the field free Λ -doublets, see eq 10, and varies as a function of the orientation field strength, the $R_1^{(1)}(\theta)$ moment is independent of the orientation field strength. Because of its dependence on $R_0^{(0)}(\theta)$, this implies that the renormalised moment, $R_1^{(1)}(\theta)/R_0^{(0)}(\theta)$, is also field dependent. This moment provides information about the preference for scattering into a specific angle as a function of the initial orientation of the NO bond-axis with respect to the x -axis. As will be discussed below in terms of the integral steric asymmetry (which is directly proportional to the renormalised $r_1^{(1)}$ moment calculated according to eq 38), the Δj dependent sign of the renormalised moment, positive and negative for even and odd Δj , respectively, corresponds to the alternation in preference for $+x$ and $-x$ orientation. Furthermore, in general the $R_1^{(1)}(\theta)$ moment has a larger magnitude in the forwards scattered direction ($\theta < 90^\circ$) than at higher scattering angles. This is concordant with the most intense features observed in the forwards scattered region of the orientation resolved DCSs in Figure 4.

5.2 Integral steric asymmetry

5.2.1 Experimental data

Comparison of the integral cross sections for the $+x$ and the $-x$ orientation allows quantification of the orientational preference observed in the experimental and simulated difference images. Figure 6a shows the experimental, QM and QCT integral steric asymmetry, calculated according to eq 36, as a function of Δj for scattering into the final e Λ -doublet: a positive/negative value corresponds to a preference for the $+x/-x$ -orientation, that is, a preference for near-side scattering towards the N-side and O-side, respectively. For comparison, the QM and QCT calculated ISAs for the z -axis orientation are shown in Figure 6b.¹³ The experimental ISA in Figure 6a exhibits pronounced oscillations between adjacent Δj values and the agreement with the QM calculations is very good. By contrast, the agreement with the QCT calculations, which predict approximately zero ISA for moderate Δj , is poor. Agreement is better at high values of Δj , where both the experiment and the QCT calculations indicate a strong preference for scattering off the N-side of the molecule. This indicates the transition from the quantum regime to the classical regime occurs around $\Delta j = 14$. Similarly to the observed preference for scattering from the N-end of the NO molecule in the end-on orientation, represented in Figure 6b,^{12,13,44,58,59} this $+x$ preference for high Δj values can be rationalised by a larger torque achievable at a larger distance from the center of mass (*i.e.* at the N-end) and necessary for high rotational excitations.^{13,34,44} Furthermore, Aoiz *et al.*⁶⁰ have shown, for collisions of NO with He, that the symmetry of the V_{sum} potential is such that trajectories which approach the N-end of the molecule are able to penetrate further into the repulsive core of the PES, resulting in more forward peaked DCSs, and consequently larger integral cross sections than for collisions at the O-end of the molecule. A similar argument can be made for scattering in the $+x$ -orientation and high Δj .

Interestingly, as the ISA switches between positive and negative values at moderate Δj ,

the oscillations are not centered around zero; in the range between $\Delta j = 4 - 11$, the $-x$ preference for even Δj is quantitatively larger than the $+x$ preference for odd Δj values. We return to this point below in Section 5.2.2.

5.2.2 Theoretical data

In order to understand the oscillatory behaviour of the ISA and the overall shift towards negative values, it is informative to consider the $R_1^{(1)}(\theta)$ moment on which, as we have seen in the preceding sections, the steric asymmetry in the side-on orientation is dependent. While the discussion here will focus on the $R_1^{(1)}(\theta)$ moment, similar arguments may be made for the $R_0^{(1)}(\theta)$ moment in the case of z -axis orientation. The $R_1^{(1)}(\theta)$ moment itself depends on the specific combinations of the field-free scattering amplitudes implicit in eq 12. We elaborate the notation for a given Δj transition and n index to

$$F_{m'\epsilon'm\epsilon}^{\Delta j,n} \equiv F_{m'\epsilon'm\epsilon} , \quad (39)$$

with

$$n = j' - \epsilon\epsilon'/2 , \quad (40)$$

which for $j = 1/2$ becomes $n = \Delta j + 1/2 - \epsilon\epsilon'/2$. For simplicity, we will assume that the different m' states behave similarly to their sum, so that in the first instance we can ignore the summation over all m' states in the expression for $R_1^{(1)}(\theta)$ in eqs 12 and 13. We have previously shown that this assumption is approximately valid (see Figure 8 in the Supplementary Information of Reference²⁸).

For transitions with $\Delta j = n$, into the final $\epsilon' = +1, e$ state, we can then define:

$$T^{\Delta j=n} = F_{m'e-1/2f}^{\Delta j,n+1} [F_{m'e1/2e}^{\Delta j,n}]^* + [F_{m'e1/2f}^{\Delta j,n+1}]^* F_{m'e-1/2e}^{\Delta j,n} . \quad (41)$$

Similarly, for a given $\Delta j = n + 1$ transition,

$$T^{\Delta j=n+1} = F_{m'e-1/2f}^{\Delta j+1,n+2} [F_{m'e-1/2e}^{\Delta j+1,n+1}]^* + [F_{m'e-1/2f}^{\Delta j+1,n+2}]^* F_{m'e-1/2e}^{\Delta j+1,n+1} . \quad (42)$$

The relation in eq 40 is just that used to describe states in so called ‘parity pairs’ in the unoriented scattering of NO with the rare gases; in which states coupled by the same term, n , have very similar DCSs.^{12,31,50,51,61} As a result of this behaviour,

$$F_{m'e-1/2f}^{\Delta j,n+1} \simeq F_{m'e-1/2e}^{\Delta j+1,n+1} . \quad (43)$$

Consequently, a change in sign between T^n and T^{n+1} (*i.e.* between $\Delta j = n$ and $\Delta j = n + 1$) is consistent with

$$F_{m'e-1/2f}^{\Delta j+1,n+2} \simeq -F_{m'e-1/2e}^{\Delta j,n} . \quad (44)$$

This is in-line with work by Stolte and coworkers,^{12,44} who have used a quasi-quantum treatment (QQT) to describe the Δj dependent oscillations in the integral steric asymmetry of end-on oriented NO molecules.

We have so far assumed that the m' components in the T expressions behave similarly, however, for the analysis to be rigorous, we have to sum over all m' values. By rotating the scattering frame into the apse frame, we can approximate the number of m' values to a single dominant one and confirm the conclusions we have drawn so far. The kinematic apse model^{62,63} assumes that the projection of the rotational angular momentum, \mathbf{j} , onto the kinematic apse

$$\hat{\mathbf{a}} = \frac{\mathbf{k} - \mathbf{k}'}{|\mathbf{k} - \mathbf{k}'|} , \quad (45)$$

is conserved during the impulsive collision between a hard sphere and a rigid ellipse.^{62,63} For NO(X) in its ground rotational state, where $j = 0.5$ and, consequently $|m_a| = 0.5$, conservation dictates that $\Delta m_a = m'_a - m_a = 0$.

The field free scattering amplitudes used in eqs 10 to 12 may be rewritten in the apse

frame according to²⁴

$$F_{m'_a \epsilon' \leftarrow m_a \epsilon}^{a, \Delta j, n}(\theta) = \sum_{m=-j}^{+j} \sum_{m'=-j'}^{+j'} F_{j' m' \epsilon' \leftarrow j m \epsilon}(\theta) d_{m m_a}^j(\beta) d_{m' m'_a}^{j'}(\beta) , \quad (46)$$

where $d_{mn}^k(\beta)$ are the Wigner rotation matrix elements, and m_a and m'_a are the projections of j and j' , respectively, onto the kinematic apse, $\hat{\mathbf{a}}$. The scattering-angle dependent apse angle, β (between \mathbf{k} and $\hat{\mathbf{a}}$), is^{64,65}

$$\cos \beta(\theta) = \frac{D - \cos \theta}{\sqrt{D^2 + 1 - 2D \cos \theta}} , \quad (47)$$

where

$$D = \sqrt{\frac{E_{\text{coll}} - \Delta E_{\text{rot}}}{E_{\text{coll}}}} , \quad (48)$$

and E_{coll} and ΔE_{rot} are the collision energy and the change in rotational energy during the collision, respectively.

Figure 7 shows the scattering amplitudes appearing in the expression for $R_1^{(1)}(\theta)$ in the apse frame, for $\Delta j = 5, \Delta j + 1 = 6$ and $\Delta j = 7, \Delta j + 1 = 8$ in the top and bottom panels, respectively. The figure only shows the real part of the scattering amplitudes, but analogous trends are observed for the imaginary parts. The plots demonstrate that the scattering amplitudes for two adjacent Δj transitions for which n is different are out-of-phase (left), while the ones for which n is equal are in-phase (right), in agreement with eqs 43 and 44. Moreover, for $\Delta j = 5, 7$ shown here, the terms that are in-phase, *i.e.* that have the same sign, are even ($n = 6, 8$ in this case), whereas the terms that have opposite sign are odd ($n = 5, 7$ and $n = 7, 9$ in Figure 7). For even Δj , the in-phase terms will have odd n , and the out-of-phase terms will be even in n .

Overall, the behavior of the scattering amplitudes shown in Figure 7 confirms that expected from consideration of the properties of the scattering amplitudes (eqs (41) to (44)), and the interpretation based on QQT theory by Stolte and coworkers.^{12,44}

The above analysis can also shed light on the electric field dependence of the integral steric asymmetry. The even terms in the potential (eqs 1, 2) are associated with parity-conserving transitions, and the odd terms in the potential are associated with parity-changing transitions. More specifically, for odd Δj transitions into the final e manifold, the $F_{m'e-1/2f}$ terms are parity-conserving, while the $F_{m'e1/2e}$ terms are parity-changing, and *vice versa* for even Δj transitions. Since NO is a nearly homonuclear molecule, the even (homonuclear) terms dominate the potential, and the odd (heteronuclear) terms are responsible for any deviations from the characteristics of a homonuclear system. This means that, for odd Δj , the $F_{m'e-1/2f}$ term dominates, while for even Δj , the $F_{m'e1/2e}$ term dominates. However, in both cases, the parity-changing term is responsible for the steric preference. At the experimental field strength, the mixing of the initial e and f states is incomplete, with the f state contributing about twice as much to the superposition as the e state. As a consequence, the nearly homonuclear character of the NO molecule is emphasized for odd Δj , for which the $F_{m'e-1/2f}$ term is parity-conserving, whereas the heteronuclear character of the molecule is emphasized for even Δj , for which $F_{m'e-1/2f}$ is parity-changing. This results in an increase in the magnitude of the steric effect for even Δj compared to odd Δj . This asymmetry, observed as a slight preference for negative S_x values, is thus a direct effect of the finite electric field strength. Figure 8 illustrates this conclusion by comparing the QM ISA obtained at the experimental electric field (left hand-side) and at infinite field strength (right hand-side). Indeed, at infinite field, as both initial states contribute equally, the ISA is approximately symmetric around zero, for transitions into both final e (top) and final f (bottom) states. For transitions into final f states at the experimental field, the ISA is shifted to more positive values, as in this case the parity-conserving and changing terms are reversed compared to the ones for the final e transitions, leading to an increase of the steric effect for odd Δj .

6 Discussion

As we have discussed in a recent paper,²⁸ in which we focused on the $\Delta j = 7 - 12$ states, the specific structures and magnitudes of the DCSs are dependent on three main factors: the strength of the experimental electric field, rotational rainbow structure arising mainly from scattering off the repulsive parts of the potential, and QM interference. The effects of the QM interference on the integral cross sections has already been discussed in the previous section. In the following sections, the role of the electric field and the characteristic features in the DCSs will be considered to elucidate the scattering process.

6.1 Field-strength dependence

In the presence of a static electric field, the initial wavefunction is a superposition of the field free e and f states, according to eq 3. Since the magnitude of the mixing parameters, α and β , see eq 4, depends on the strength of the applied field, the ratio of the e and f Λ -doublets in the superposition also depends on the field strength. At the end of Section 5.2.2 we have already considered how the field strength influences the integral steric asymmetry, and it is also informative to consider how the DCSs calculated at the experimental field strength (9.2 kV cm^{-1}), where $|\alpha| = 0.64$ and $|\beta| = 1.26$, compare to the infinite field case, where $|\alpha| = |\beta| = 1$. Figure 9 shows the QM x -axis orientation resolved DCSs at the experimental and infinite fields for scattering of NO(X) with Ar into the final $|j', \Omega' = 0.5, \epsilon'\rangle$ states. The states presented here have been chosen for clarity, however the trends which will be discussed persist for all but very high rotational states where the DCSs are very backwards scattered. At infinite field, only the final e state is plotted, as scattering into either final Λ -doublet is approximately equivalent in this limit.

Consider first the DCSs at infinite field strength (first column in Figure 9), where there is a 1:1 ratio of the $e:f$ Λ -doublets in the initial superposition of states; two major trends are observed in the DCSs. The integral steric effect is again obvious to see, with a preference

for scattering in the $+x$ -orientation for odd Δj , and the $-x$ -orientation for even Δj . The second trend is a propensity for multiple peaks in the $+x$ -orientation and single peaks in the $-x$ -orientation, irrespective of the final Δj value. In each case, the lowest scattering angle peak in the $+x$ -orientation is more forwards scattered than the single peak in the $-x$ -orientation.

Now consider the DCSs calculated at the experimental field strength (second/third columns for final f/e states). As in the infinite field case, a single peak is observed in the $-x$ -orientation for all states, however, the multiple peaks in the $+x$ -orientation are no longer obvious for all states. For scattering into the final e state, multiple peaks are only observed for odd Δj (possibly with a hint of a second peak for even Δj), whilst in the final f state, multiple peaks are observed more clearly for even Δj and the second peak is less pronounced for odd Δj .

The trends in the experimental field may be rationalised by considering again the relative magnitude of the mixing parameters in the superposition of states in eq 3. As the strength of the field tends towards zero, the DCS for both the $+x$ - and $-x$ -orientations evolves toward that observed in the field free state (*i.e.* $f \rightarrow e$ for transitions into the final e Λ -doublet). In the field-free case, it is well known that parity plays an important role in the structure observed in the DCS; where parity conserving and changing transitions result in multiple and single peaks in the DCS, respectively.^{50,53,66} The field free DCSs for transitions to the final e states are shown in the last column in Figure 9. It has already been mentioned that at the experimental field strength, the ratio of the contributions from the initial f and e states is approximately 2:1. Odd Δj transitions from $f \rightarrow e$ are parity conserving, while the corresponding even Δj transitions are parity changing. Therefore, the stronger contribution of the parity conserving scattering amplitude gives rise to multiple peaks in the $+x$ -orientation for odd Δj , but single peaks for even Δj . The opposite is true for the final f state. Thus, even though the initial wavefunction of the NO molecule does not *per se* possess a well-defined parity, the parities associated with the contributing scattering amplitudes play

a crucial role in determining both the integral and the differential cross sections.

6.2 QM and QCT calculations at infinite field

Figure 10 compares the fixed collision energy QM bond-axis orientation resolved DCSs for the $|j', \Omega' = 0.5, \epsilon' = 1, e\rangle \leftarrow |j = 0.5, \Omega = 0.5, E = \infty\rangle$ transitions populated by NO(X) + Ar scattering with the corresponding QCT data. Given the field dependence of the observed integral and differential steric effects, all calculations were run at infinite field to remove any effects arising from the incomplete mixing of the field-free states in the (orientation) field. The renormalised $R_1^{(1)}(\theta)$ moments ($R_1^{(1)}(\theta)/R_0^{(0)}(\theta)$) are also shown (third column), as well as QM and QCT simulations of the experimental images (fourth column). Note that the limits of the renormalised moments depend on the mixing parameters, α and β , and therefore on the field strength according to $\pm 1/|\alpha\beta|$; the limits are therefore ± 1 at infinite field, and ± 1.24 at the experimental field. For each pair of $\pm x$ images, the intensity scale is equivalent as to conserve the relative intensities between the two (*i.e.* the integral steric effect).

For low $\Delta j (= 2)$ transitions, the DCSs and corresponding (simulated) ion images are strongly forwards scattered. An ℓ -type rainbow^{49,55,67} is observed as a secondary peak in the QCT $-x$ DCS for $\Delta j = 2$, corresponding to attractive far-side scattering off the N-side of the molecule; this arises from the larger extent of the attractive part of the potential at the N-end, than at the O-end, of the molecule. Since the final relative velocity vector for far-side scattering on the N-side lies in the same hemisphere as the vector for near-side scattering from the O-side, the intensity arising from the rainbow contributes to the $-x$ integral cross section, resulting in an apparent preference for this orientation and a corresponding dip in the QCT ISA (Figure 6). Any signs of this secondary maximum in the corresponding QM calculations are washed out by strong glory scattering and the presence of diffraction oscillations which are superimposed over the general structure of the DCS. The QM renormalised $R_1^{(1)}(\theta)$ moment is strongly dependent on the scattering angle, whilst only a single peak is observed

in the QCT moment (at the angle of the ℓ -type rainbow), confirming that the deviation from the otherwise negligible steric effect in the QCT data is mainly due to the rainbow. It should also be noted that whilst structure is observed in the QM moment, the actual cross section for scattering beyond $\theta \approx 30^\circ$ is very small in magnitude and the orientation resolved DCSs are essentially zero in this region. The strongly forwards scattered nature of the DCSs are obvious from the QM and QCT simulations, with very similar structure in both cases. The secondary maximum in the $-x$ QCT DCS is unresolved in the corresponding simulated image due to the use in the simulations of the experimental resolution.

The consecutive transitions with moderate Δj ($= 5, 6$ and $11, 12$) in Figure 10 show generally poor agreement between the QM and QCT data, which is not surprising given the disparity between the QCT and experimental integral steric asymmetries in Figure 6. Mostly single peaks with some structure are observed for both orientations in the QCT data, with the $+x$ DCS being more forwards scattered than the $-x$ DCS. Again, this is simple to rationalise classically; collisions off the N-side are possible at larger impact parameters than for collisions off the O-side, as the N-end extends further from the center of mass than the O-end of the molecule. These larger impact parameters, for which collisions are more glancing in nature, result in smaller deflection angles for N-side collisions than for O-side collision for scattering into the same final rotational state. The additional structure in the QCT DCSs arises due to the bond-axis distribution created in the orientation field (illustrated in Figure 2), which has contributions from collisions at either end of the NO molecule (with lower probabilities than for the side-on orientation of interest), resulting in shoulders on the main peak in the DCS.³⁴

The QCT simulated images for the $\pm x$ -orientations for these intermediate states look very similar, consistent with the similar magnitudes in their DCSs and the resulting negligible steric effect shown in Figure 6. In contrast, the two sides in the simulated QM images exhibit varying intensities. Analogous to the trend in the QCT data, and for the same reasons, the $+x$ QM DCSs are more forwards scattered than the corresponding $-x$ DCSs.

Prior work²⁸ has shown that the characteristic QM distributions for the $\pm x$ -orientations arise from different rotational rainbow structure associated with repulsive scattering from the inherently anisotropic PES.^{47,51,67–70} Classically, such scattering results in a sharp peak in the DCS at the so-called ‘rainbow angle’, below which scattering is forbidden, as there is insufficient incoming translational energy to reach the rotational state of interest. The additional structure in the QM DCS may be rationalised using a simple ‘two-path’ model,²⁸ in which interference between trajectories leading to the same scattering angle but which scatter from the end and side of the molecule is invoked. In this model, the phase difference between two interfering trajectories (or paths) is smaller at the N-end/side than at the O-end/side, leading to more peaks and smaller scattering angles in the corresponding DCS.

The QCT and QM renormalised $R_1^{(1)}(\theta)$ moments do not depend on the magnitude of the angular scattering distributions, and consequently allow direct comparison of the classical and QM steric effect without the complication of underlying differences in the angular scattering distributions. From eqs 36 and 37, it follows that a positive $R_1^{(1)}(\theta)$ moment corresponds to a preference for the $+x$ orientation (and a positive steric asymmetry), and *vice versa* for negative values of $R_1^{(1)}(\theta)$. As noted for the DCSs, for intermediate Δj , the agreement between the QCT and QM calculations is poor. The QCT moment is slightly negative for the most part, except for the region below $\approx \theta = 40^\circ$, where the moment shows a positive peak, corresponding to a modest preference for the $+x$ -orientation. However, the QM moment is largely positive/negative for odd/even Δj , respectively, as expected from the Δj dependent oscillations in the integral steric effect. As Δj increases, the moments become more backwards scattered. For the Δj transitions between 5 and 12, the magnitude of the moment is greatest in the most forwards scattered region, in line with the overall preference for forwards scattering. In general, the QCT moment peaks in a similar region to the QM moment, but is close to zero at higher scattering angles.

Collisions which result in large rotational energy transfer are largely ‘head-on’ in nature, resulting in DCSs which are dominated by backwards scattering. The QCT and QM x -axis

DCSs for $\Delta j = 15$ are in relatively good qualitative agreement, indicating that the collision mechanism for high rotational excitations can be largely described in classical terms, with collisions off the N-side dominating. A single peak is observed in both the $\pm x$ DCSs, with the $+x$ DCS being more forwards scattered than the $-x$ DCS and the $+x$ DCS also having a larger magnitude than the $-x$ DCS. The agreement between QM and QCT is also good for the renormalised $R_1^{(1)}(\theta)$ moment, as well as for the simulations. A subtle difference in the relative intensities of the images is observed between the QM and QCT simulations, since $S_x^{\text{QM}} > S_x^{\text{QCT}}$ (see Figure 6a).

The comparison between the QM and QCT data for different Δj transitions clearly shows that the NO + Ar collision system is predominantly quantum mechanical in the low to middle Δj region, but enters the classical regime around $\Delta j = 14$, where the agreement between the QM and QCT data is qualitatively very reasonable.

6.3 Mechanistic insights

Figure 11 shows the QM differential cross sections calculated at infinite field for the x -axis orientation (top row) and for the z -axis orientation (middle row) for $\Delta j = 2, 5, 6, 11, 12, 15$ into the final e Λ -doublet. The $+x/-x$ DCSs are represented by red and blue (dashed) lines, and the $+z/-z$ DCSs by purple (dashed) and green lines. Note that collisions at the N-end are ‘ $-z$ ’ and collision at the O-end are ‘ $+z$ ’, whilst collisions towards the N-side and O-side are ‘ $+x$ ’ and ‘ $-x$ ’, respectively. Also shown are the maximised DCSs (grey shaded area), which, for a given scattering angle, represent the maximally possible scattering intensity when the molecule is allowed to take on any arbitrary orientation. The cartoons in the bottom row for each final state show the NO orientation that maximises the DCS at two selected scattering angles, indicated as (a) and (b) above the corresponding DCSs. The shaded regions represent the initial bond-axis distribution created at infinite electric field and the sketch of the NO molecule depicts the most probable orientation. Red is used to indicate an N-end/side preference, whilst blue indicates an O-end/side preference.

The DCSs for $\Delta j = 2$ are very forwards scattered and show similar structures in both the end-on and the side-on orientations. For very low rotational excitations, collisions are very much glancing in nature and the specific structures of the DCSs are strongly dependent on the topography of the attractive region of the potential energy surface, with far-side scattering being the dominant pathway. The strong oscillations in the very forward scattered region for $\Delta j = 2$ are due to molecular diffraction.^{24,71} Close to $\theta = 0$ (a), the DCS is maximised in a nearly N-end geometry, but the differences between the four geometries ($\pm x, \pm z$) are very small. For large scattering angles (b), the preference is for O-end collisions, but the overall scattering intensity is negligibly small. Overall, there is a slight preference for $-x$ and N-end collisions in the side-on and end-on configurations, respectively. This behaviour reflects a deviation from the general trend observed at intermediate and high Δj , for which a preference for $+x/-x$ orientation coincides with the preference for N-end/O-end collisions, for odd and even Δj , respectively. This deviation suggests inherent differences between the scattering dynamics for very low ($\Delta j = 1 - 3$) and for intermediate and high rotational transitions ($\Delta j \geq 4$). The differences are likely due to the dominance of the attractive (and therefore the presence of far-side scattering) and the repulsive parts in the former and the latter case, respectively.

As shown previously for $\Delta j = 7$ and 8,²⁸ the $+x$ DCS for $\Delta j = 5$ and the $-x$ DCS for $\Delta j = 6$ almost perfectly match the corresponding maximised DCSs. The preference for $+x$ in the former and for $-x$ in the latter case again reflects the alternation of the integral steric asymmetry discussed above. In contrast to the x -axis DCSs, the z -axis oriented DCSs are significantly smaller in the most intense forward scattered region than the maximised DCSs. Moreover, the differences between the two orientations are much less pronounced than for x -axis orientation, although the alternation in the ISA as a function of the Δj transition is observed as well (see Figure 6b). This comparison highlights two points: firstly, the much larger difference in the magnitude of the $\pm x$ DCSs compared to the $\pm z$ DCSs shows that significantly more control over the scattering intensity may be achieved by orienting the

NO molecule side-on rather than end-on. Secondly, the similarity of the x -axis orientation and the maximised DCS suggests that the preferred collision mechanisms involves a side-on geometry. The cartoons below the DCSs show that at low scattering angles in the very forwards direction (a), where the majority of the scattering intensity is observed, the orientation that maximises the DCS is mostly side-on, while at large scattering angles (b), where the magnitude of the DCS is much smaller, the preferred orientation is an end-on configuration. A similar picture emerges for scattering into higher Δj ($=11, 12, 15$), shown in the lower part of Figure 11; a preference for side-on and end-on collisions is observed for more forward (a) and backward (b) scattering, respectively. However, as the signal intensity is shifted to the region above $\theta = 90^\circ$, the end-on orientation becomes more important for these higher rotational excitations. The difference between the dominant $-z$ DCS and the $+z$ DCS in the backwards scattered region for $\Delta j = 12, 15$ is also much larger than for the two x -axis orientations, indicating substantial control over the scattering outcome in the end-on geometry for these higher lying rotational states. This implies that the preferred collision geometry (side-on *vs.* end-on) is also the geometry in which the collision outcome (*i.e.* the magnitude of the DCS) can be maximally controlled.

The preference for side-on and end-on scattering into smaller and larger angles, respectively, makes intuitive sense: for high rotational excitation, the collision must necessarily be more impulsive than for glancing-blow collisions resulting in low rotational excitation. In the end-on orientation, head-on collisions with small impact parameters efficiently lead to predominantly backward scattered trajectories, whilst smaller impact parameter collisions with side-on oriented molecules are less impulsive, due to the extended attractive regions on the side of the molecule. On the other hand, side-on orientation allows for large impact parameter collisions which result in small-angle scattering.

7 Conclusions and Outlook

We have presented experimental and computational results and a thorough analysis of the inelastic scattering of NO with Ar in which the NO bond-axis is oriented side-on to the incoming collision partner. Orientation of the bond-axis was achieved by exposing hexapole state selected NO molecules to a static electric field directed perpendicular to the initial relative velocity, \mathbf{k} , of the collision system. Due to the breaking of symmetry about \mathbf{k} in this orientation, a data analysis method extracting the relevant polarisation moments (r -PDDCS) from the sum and difference of the $\pm x$ -orientation images was used, allowing determination of the experimental orientation resolved DCSs, as well as the experimental integral steric asymmetry. The agreement between experiment and QM calculations was shown to be very good.

The strength of the orientation field was shown to be important in rationalising the structure observed in the orientation resolved DCSs; at the experimental field the incomplete mixing of the initial Λ -doublets prior to the collision leads to multiple peaks in the $+x$ DCSs of transitions with odd Δj , whilst single peaks are observed in all other cases. This is attributed to the parity of the individual transitions from the e and f states, which are mixed upon application of the orientation field. It was shown that at infinite field, at which there is a 1:1 ratio of the initial e and f Λ -doublets, multiple peaks are observed for all $+x$ DCSs and single peaks for all $-x$ DCSs.

Classical and quantum calculations showed that the structure observed in the experimental DCSs cannot be explained using a classical model, except at the very highest Δj where classical arguments based around ‘torque’ are important. The larger impact parameter collisions possible on the side of the molecule result in an overall preference for the side-on orientation in the forward scattered region, whilst at higher scattering angles, the QM calculations suggest a preference for the end-on orientation. As the potential probed in the side-on geometry is asymmetric around the approach direction of the Ar atom, the two side-on orientations show very distinct structures in their DCSs. Trajectories towards the

N-side ($+x$) allow for higher impact parameter collisions, resulting in more forward scattered DCSs with multiple peaks, whilst trajectories towards the O-side ($-x$) have smaller impact parameters, leading to higher scattering angles and single peaks in the DCSs.

Extension of the current experiment, using circularly polarised light to detect the rotationally excited NO molecules, would allow measurement of the bond orientation resolved collision induced orientation, *i.e.* the effect of bond orientation on the sense of rotation of the final rotational angular momentum, \mathbf{j}' ; ^{72,73} the full four-vector $\mathbf{r} - \mathbf{k} - \mathbf{k}' - \mathbf{j}'$ correlation. The strong steric effect in the side-on orientation is expected to also be observed for this higher-order correlation. Collision induced alignment (measured using linearly polarised light), on the other hand, is not expected to depend strongly on the bond-axis orientation, due to the largely classical mechanisms observed in the unoriented case. ^{37,39,74,75}

8 Acknowledgement

The support of the UK EPSRC (to M.B. *via* Programme Grant EP/L005913/1) and the Spanish Ministry of Science and Innovation (to F.J.A. *via* grants MINECO/FEDERCTQ2015-65033-P, and PGC2018-09644-B-100) is gratefully acknowledged. P.G.J. acknowledges funding by Fundación Salamanca City of Culture and Knowledge (Programme for attracting scientific talent to Salamanca).

References

- (1) Curran, D. P.; Porter, N. A.; Giese, B. *Stereochemistry of Radical Reactions: Concepts, Guidelines, and Synthetic Applications*; John Wiley & Sons: New York, 2008.
- (2) Cash, J. M.; Heal, M. R.; Langford, B.; Drewer, J. A review of stereochemical implications in the generation of secondary organic aerosol from isoprene oxidation. *Environ. Sci.: Processes Impacts* **2016**, *18*, 1369–1380.
- (3) Vaultier, F.; Monteil, V.; Spitz, R.; Thuilliez, J.; Boisson, C. New insights on Ni-based catalysts for stereospecific polymerization of butadiene. *Polym. Chem.* **2012**, *3*, 1490–1494.
- (4) Wang, F.; Lin, J.; Liu, K. Steric control of the reaction of CH stretch-excited CHD₃ with chlorine atoms. *Science* **2011**, *331*, 900–903.
- (5) Wang, F.; Liu, K.; Rakitzis, T. P. Revealing the stereospecific chemistry of the reaction of Cl with aligned CHD₃($v_1=1$). *Nat. Chem.* **2012**, *4*, 636–641.
- (6) Pan, H.; Wang, F.; Czako, G.; Liu, K. Direct mapping of the angle-dependent barrier to reaction for Cl + CHD₃ using polarized scattering data. *Nat. Chem.* **2017**, *9*, 1175–1180.
- (7) Sharples, T. R.; Leng, J. G.; Luxford, T. F. M.; McKendrick, K. G.; Jambrina, P. G.; Aoiz, F. J.; Chandler, D. W.; Costen, M. L. Non-intuitive rotational reorientation in collisions of NO(A²Σ⁺) with Ne from direct measurement of a four-vector correlation. *Nat. Chem.* **2018**, *10*, 1148–1153.
- (8) Perreault, W. E.; Mukherjee, N.; Zare, R. N. Cold quantum-controlled rotationally inelastic scattering of HD with H₂ and D₂ reveals collisional partner reorientation. *Nat. Chem.* **2018**, *10*, 561–567.

- (9) Jones, E. M.; Brooks, P. R. Focusing and orienting asymmetric-top molecules in molecular beams. *J. Chem. Phys.* **1970**, *53*, 55–58.
- (10) Loesch, H. J.; Remscheid, A. Brute force in molecular reaction dynamics: A novel technique for measuring steric effects. *J. Chem. Phys.* **1990**, *93*, 4779–4790.
- (11) van Leuken, J.; Bulthuis, J.; Stolte, S.; Snijders, J. Steric asymmetry in rotationally inelastic state-resolved NO-Ar collisions. *Chem. Phys. Lett.* **1996**, *260*, 595–603.
- (12) Gijsbertsen, A.; Linnartz, H.; Taatjes, C. A.; Stolte, S. Quantum interference as the source of steric asymmetry and parity propensity rules in NO-rare gas inelastic scattering. *J. Am. Chem. Soc.* **2006**, *128*, 8777–8789.
- (13) Nichols, B.; Chadwick, H.; Gordon, S. D. S.; Eyles, C. J.; Hornung, B.; Brouard, M.; Alexander, M. H.; Aoiz, F. J.; Gijsbertsen, A.; Stolte, S. Steric effects and quantum interference in the inelastic scattering of NO(X) + Ar. *Chem. Sci.* **2015**, *6*, 2202–2210.
- (14) Boca, A.; Friedrich, B. Fine structure, alignment, and orientation of $^{32}\text{S}^{16}\text{O}$ and $^{16}\text{O}^{18}\text{O}$ molecules in congruent electric and magnetic fields. *J. Chem. Phys.* **2000**, *112*, 3609–3619.
- (15) Zou, J.; Gordon, S. D. S.; Tanteri, S.; Osterwalder, A. Stereodynamics of $\text{Ne}(^3\text{P}_2)$ reacting with Ar, Kr, Xe, and N_2 . *J. Chem. Phys.* **2018**, *148*, 164310.
- (16) Gordon, S. D. S.; Omiste, J. J.; Zou, J.; Tanteri, S.; Brumer, P.; Osterwalder, A. Quantum-state-controlled channel branching in cold $\text{Ne}(^3\text{P}_2)+\text{Ar}$ chemi-ionization. *Nat. Chem.* **2018**, *10*, 1190–1195.
- (17) Perreault, W. E.; Mukherjee, N.; Zare, R. N. Quantum control of molecular collisions at 1 kelvin. *Science* **2017**, *358*, 356–359.
- (18) de Lange, M.; Drabbels, M.; Griffiths, P.; Bulthuis, J.; Stolte, S.; Snijders, J. Steric asymmetry in state-resolved NO–Ar collisions. *Chem. Phys. Lett.* **1999**, *313*, 491–498.

- (19) Friedrich, B.; Herschbach, D. R.; Rost, J.-M.; Rubahn, H.-G.; Renger, M.; Verbeek, M. Optical spectra of spatially oriented molecules: ICl in a strong electric field. *J. Chem. Soc., Faraday Trans.* **1993**, *89*, 1539–1549.
- (20) Jankunas, J.; Reisman, K. S.; Rakitzis, T. P.; Osterwalder, A. Oriented O(3P_2), Ne(3P_2), and He(3S_1) atoms emerging from a bent magnetic guide. *Mol. Phys.* **2016**, *114*, 245–252.
- (21) Gilijamse, J. J.; Hoekstra, S.; van de Meerakker, S. Y. T.; Groenenboom, G. C.; Meijer, G. Near-threshold inelastic collisions using molecular beams with a tunable velocity. *Science* **2006**, *313*, 1617–1620.
- (22) Vogels, S. N.; Onvlee, J.; Chefdeville, S.; van der Avoird, A.; Groenenboom, G. C.; van de Meerakker, S. Y. T. Imaging resonances in low-energy NO-He inelastic collisions. *Science* **2015**, *350*, 787–790.
- (23) Onvlee, J.; Vogels, S. N.; van de Meerakker, S. Y. T. Unraveling cold molecular collisions: Stark decelerators in crossed-beam experiments. *Chem. Phys. Chem.* **2016**, *17*, 3583–3595.
- (24) Onvlee, J.; Gordon, S. D. S.; Vogels, S. N.; Auth, T.; Karman, T.; Nichols, B.; van der Avoird, A.; Groenenboom, G. C.; Brouard, M.; van de Meerakker, S. Y. T. Imaging quantum stereodynamics through Fraunhofer scattering of NO radicals with rare-gas atoms. *Nat. Chem.* **2016**, *9*, 226–233.
- (25) Ni, K.-K.; Ospelkaus, S.; Wang, D.; Quémener, G.; Neyenhuis, B.; de Miranda, M. H. G.; Bohn, J. L.; Ye, J.; Jin, D. S. Dipolar collisions of polar molecules in the quantum regime. *Nature* **2010**, *464*, 1324–1328.
- (26) Ospelkaus, S.; Ni, K.-K.; Wang, D.; de Miranda, M. H. G.; Neyenhuis, B.; Quémener, G.; Julienne, P. S.; Bohn, J. L.; Jin, D. S.; Ye, J. Quantum-state con-

- trolled chemical reactions of ultracold potassium-rubidium molecules. *Science* **2010**, *327*, 853–857.
- (27) de Miranda, M. H. G.; Chotia, A.; Neyenhuis, B.; Wang, D.; Quémener, G.; Ospelkaus, S.; Bohn, J. L.; Ye, J.; Jin, D. S. Controlling the quantum stereodynamics of ultracold bimolecular reactions. *Nat. Phys.* **2011**, *7*, 502–507.
- (28) Heid, C. G.; Walpole, V.; Brouard, M.; Aoiz, F. J.; Jambrina, P. G. Side-impact collisions of Ar with NO. *Nat. Chem.* **2019**, *11*, 662–668.
- (29) Alexander, M. H. Rotationally inelastic collisions between a diatomic molecule in a $^2\Pi$ electronic state and a structureless target. *J. Chem. Phys.* **1982**, *76*, 5974–5988.
- (30) Alexander, M. H. Differential and integral cross sections for the inelastic scattering of NO($X^2\Pi$) by Ar based on a new *ab initio* potential energy surface. *J. Chem. Phys.* **1993**, *99*, 7725–7738.
- (31) Alexander, M. H. A new, fully *ab initio* investigation of the NO($X^2\Pi$) Ar system. I. Potential energy surfaces and inelastic scattering. *J. Chem. Phys.* **1999**, *111*, 7426–7434.
- (32) Alexander, M. H.; Stolte, S. Investigation of steric effects in inelastic collisions of NO($X^2\Pi$) with Ar. *J. Chem. Phys.* **2000**, *112*, 8017–8026.
- (33) Aoiz, F. J.; Brouard, M.; Gordon, S. D. S.; Nichols, B.; Stolte, S.; Walpole, V. A new perspective: imaging the stereochemistry of molecular collisions. *Phys. Chem. Chem. Phys.* **2015**, *17*, 30210–30228.
- (34) Brouard, M.; Chadwick, H.; Gordon, S. D. S.; Hornung, B.; Nichols, B.; Aoiz, F. J.; Stolte, S. Stereodynamics in NO(X) + Ar inelastic collisions. *J. Chem. Phys.* **2016**, *144*, 224301.

- (35) Aoiz, F. J.; Martínez, M. T.; Sáez-Rábanos, V. Quasi-classical treatment of the stereodynamics of chemical reactions: $\mathbf{k-r-k'}$ vector correlation for the $\text{Li}+\text{HF}(v=1,j=1) \rightarrow \text{LiF}+\text{H}$ reaction. *J. Chem. Phys.* **2001**, *114*, 8880–8896.
- (36) Aoiz, F. J.; Herrero, V. J.; Sáez-Rábanos, V.; Verdasco, J. E. Classical stereodynamics in $\text{Ar} + \text{NO}$ inelastic collisions. *Phys. Chem. Chem. Phys.* **2004**, *6*, 4407–4415.
- (37) Brouard, M.; Chadwick, H.; Eyles, C. J.; Hornung, B.; Nichols, B.; Aoiz, F. J.; Jambolina, P. G.; Stolte, S. Rotational alignment effects in $\text{NO(X)} + \text{Ar}$ inelastic collisions: An experimental study. *J. Chem. Phys.* **2013**, *138*, 104310.
- (38) Brouard, M.; Chadwick, H.; Eyles, C. J.; Hornung, B.; Nichols, B.; Scott, J. M.; Aoiz, F. J.; Klos, J.; Stolte, S.; Zhang, X. The fully quantum state-resolved inelastic scattering of $\text{NO(X)} + \text{Ne}$: experiment and theory. *Mol. Phys.* **2013**, *111*, 1759–1771.
- (39) Brouard, M.; Chadwick, H.; Gordon, S. D. S.; Hornung, B.; Nichols, B.; Klos, J.; Aoiz, F. J.; Stolte, S. Fully quantum state-resolved inelastic scattering of $\text{NO(X)} + \text{Kr}$: Differential cross sections and product rotational alignment. *J. Chem. Phys.* **2014**, *141*, 164306.
- (40) Stolte, S. Reactive scattering studies on oriented molecules. *Ber. Bunsenges. Phys. Chem.* **1982**, *86*, 413–421.
- (41) Parker, D. H.; Jalink, H.; Stolte, S. Dynamics of molecular stereochemistry *via* oriented molecule scattering. *J. Phys. Chem.* **1987**, *91*, 5427–5437.
- (42) Parker, D. H.; Bernstein, R. B. Oriented molecule beams *via* the electrostatic hexapole - preparation, characterization, and reactive scattering. *Annu. Rev. Phys. Chem.* **1989**, *40*, 561–595.
- (43) Gijsbertsen, A.; Linnartz, H.; Rus, G.; Wiskerke, A. E.; Stolte, S.; Chandler, D. W.;

- Kłos, J. Differential cross sections for collisions of hexapole state-selected NO with He. *J. Chem. Phys.* **2005**, *123*, 224305.
- (44) Brouard, M.; Gordon, S. D. S.; Hackett Boyle, A.; Heid, C. G.; Nichols, B.; Walpole, V.; Aoiz, F. J.; Stolte, S. Integral steric asymmetry in the inelastic scattering of NO($X^2\Pi$). *J. Chem. Phys.* **2017**, *146*, 014302.
- (45) Eppink, A. J. B.; Parker, D. H. Velocity map imaging of ions and electrons using electrostatic lenses: Application in photoelectron and photofragment ion imaging of molecular oxygen. *Rev. Sci. Instrum.* **1997**, *68*, 3477–3484.
- (46) Chandler, D. W.; Houston, P. L. Two-dimensional imaging of state-selected photodissociation products detected by multiphoton ionization. *J. Chem. Phys.* **1987**, *87*, 1445–1447.
- (47) Alexander, M. H. A new, fully *ab initio* investigation of the ArNO($X^2\Pi$) system. II. Bound states of the Ar–NO complex. *J. Chem. Phys.* **1999**, *111*, 7435–7439.
- (48) HIBRIDON is a package of programs for the time-independent quantum treatment of inelastic collisions and photodissociation written by M. H. Alexander, D. E. Manolopoulos, H. Werner and B. Follmeg, with contributions by P. F. Vohralik, D. Lemoine, G. Corey, R. Gordon, B. Johnson, T. Orlikowski, A. Berning, A. D. Esposti, C. Rist, P. Dagdigian, B. Pouilly, G. van der Sanden, M. Yang, F. de Weerd, S. Gregurick and J. Kłos.
- (49) Aoiz, F. J.; Verdasco, J. E.; Herrero, V. J.; Sáez-Rábanos, V.; Alexander, M. A. Attractive and repulsive interactions in the inelastic scattering of NO by Ar: A comparison between classical trajectory and close-coupling quantum mechanical results. *J. Chem. Phys.* **2003**, *119*, 5860–5866.
- (50) Eyles, C. J.; Brouard, M.; Yang, C.; Kłos, J.; Aoiz, F. J.; Gijsbertsen, A.;

- Wiskerke, A. E.; Stolte, S. Interference structures in the differential cross-sections for inelastic scattering of NO by Ar. *Nat. Chem.* **2011**, *3*, 597–602.
- (51) Eyles, C. J.; Brouard, M.; Chadwick, H.; Aoiz, F. J.; Kłos, J.; Gijbbers, A.; Zhang, X.; Stolte, S. The effect of parity conservation on the spin–orbit conserving and spin–orbit changing differential cross sections for the inelastic scattering of NO(X) by Ar. *Phys. Chem. Chem. Phys.* **2012**, *14*, 5420–5439.
- (52) Zare, R. N. *Angular Momentum*; Wiley-Interscience: New York, 1987.
- (53) Eyles, C. J.; Brouard, M.; Chadwick, H.; Hornung, B.; Nichols, B.; Yang, C.-H.; Kłos, J.; Aoiz, F. J.; Gijbbers, A.; Wiskerke, A. E. *et al.* Fully Λ -doublet resolved state-to-state differential cross-sections for the inelastic scattering of NO(X) with Ar. *Phys. Chem. Chem. Phys.* **2012**, *14*, 5403–5419.
- (54) Bass, M. J.; Brouard, M.; Clark, A. P.; Vallance, C. Fourier moment analysis of velocity-map ion images. *J. Chem. Phys.* **2002**, *117*, 8723–8735.
- (55) Chadwick, H.; Nichols, B.; Gordon, S. D. S.; Hornung, B.; Squires, E.; Brouard, M.; Kłos, J.; Alexander, M. H.; Aoiz, F. J.; Stolte, S. Inelastic scattering of NO by Kr: Rotational polarization over a rainbow. *J. Phys. Chem. Lett.* **2014**, *5*, 3296–3301.
- (56) Brouard, M.; Chadwick, H.; Eyles, C. J.; Hornung, B.; Nichols, B.; Aoiz, F. J.; Jambolina, P. G.; Stolte, S.; de Miranda, M. P. Rotational alignment effects in NO(X) + Ar inelastic collisions: A theoretical study. *J. Chem. Phys.* **2013**, *138*, 104309.
- (57) van Beek, M. C.; ter Meulen, J. J.; Alexander, M. H. Rotationally inelastic collisions of OH($X^2\Pi$)+Ar. II. The effect of molecular orientation. *J. Chem. Phys.* **2000**, *113*, 637–646.
- (58) Alexander, M. H. Polarization and steric effects in inelastic collisions of NO($X^2\Pi$) with Ar and He. *Faraday Discuss.* **1999**, *113*, 437–454.

- (59) Gijsbertsen, A.; Linnartz, H.; Kłos, J.; Stolte, S. What is wrong with the steric asymmetry in atom-molecule collisions? *Phys. Scr.* **2005**, *72*, C1–C5.
- (60) Aoiz, F. J.; Verdasco, J. E.; Brouard, M.; Kłos, J.; Marinakis, S.; Stolte, S. Inelastic scattering of He atoms and NO($X^2\Pi$) molecules: The role of parity on the differential cross section. *J. Phys. Chem. A* **2009**, *113*, 14636–14649.
- (61) Kłos, J.; Aoiz, F. J.; Verdasco, J. E.; Brouard, M.; Marinakis, S.; Stolte, S. Fully quantum state-resolved inelastic scattering between He and NO($X^2\Pi$). *J. Chem. Phys.* **2007**, *127*, 031102.
- (62) Khare, V.; Kouri, D. J.; Hoffman, D. K. On j_z -preserving propensities in molecular collisions. I. Quantal coupled states and classical impulsive approximations. *J. Chem. Phys.* **1981**, *74*, 2275–2286.
- (63) Hoffman, D. K.; Evans, J. W.; Kouri, D. J. The kinematic apse and j_z -preserving propensities for nonreactive, dissociative, and reactive polyatomic collisions. *J. Chem. Phys.* **1984**, *80*, 144–148.
- (64) Ballast, A.; Gijsbertsen, A.; Linnartz, H.; Stolte, S. The quasi-quantum treatment of rotationally inelastic scattering from a hard shell potential: its derivation and practical use. *Mol. Phys.* **2008**, *106*, 315–331.
- (65) Meyer, H. State-resolved cross-sections and collision-induced alignment from counter-propagating beam scattering of $\text{NH}_3 + \text{He}$. *J. Phys. Chem.* **1995**, *99*, 1101–1114.
- (66) Taatjes, C. A.; Gijsbertsen, A.; de Lange, M. J. L.; Stolte, S. Measurements and quasi-quantum modeling of the steric asymmetry and parity propensities in state-to-state rotationally inelastic scattering of NO ($^2\Pi_{1/2}$) with D₂. *J. Phys. Chem. A* **2007**, *111*, 7631–7639.

- (67) Schinke, R.; Korsch, H. J.; Poppe, D. Rainbows in rotationally inelastic scattering: A comparative study of different model potential surfaces and dynamical approximations. *J. Chem. Phys.* **1982**, *77*, 6005–6020.
- (68) Bowman, J. M. Rotational rainbows in inelastic atom-molecule differential cross sections. *Chem. Phys. Lett.* **1979**, *62*, 309 – 311.
- (69) Bontuyan, L. S.; Suits, A. G.; Houston, P. L.; Whitaker, B. J. State-resolved differential cross-sections for crossed-beam Ar-NO inelastic-scattering by direct ion imaging. *J. Phys. Chem.* **1993**, *97*, 6342–6350.
- (70) Dixit, A. A.; Pisano, P. J.; Houston, P. L. Differential cross section for rotationally inelastic scattering of vibrationally excited NO($v=5$) from Ar. *J. Phys. Chem. A* **2001**, *105*, 11165–11170.
- (71) Leshko, M.; Friedrich, B. An analytic model of the stereodynamics of rotationally inelastic molecular collisions. *Phys. Chem. Chem. Phys.* **2010**, *12*, 1038–1041.
- (72) Lorenz, K. T.; Chandler, D. W.; Barr, J. W.; Chen, W.; Barnes, G. L.; Cline, J. I. Direct measurement of the preferred sense of NO rotation after collision with Argon. *Science* **2001**, *293*, 2063–2066.
- (73) Brouard, M.; Chadwick, H.; Gordon, S. D. S.; Hornung, B.; Nichols, B.; Aoiz, F. J.; Stolte, S. Rotational orientation effects in NO(X) + Ar inelastic collisions. *J. Phys. Chem. A* **2015**, *119*, 12404–12416.
- (74) Cline, J. I.; Lorenz, K. T.; Wade, E. A.; Barr, J. W.; Chandler, D. W. Ion imaging measurement of collision-induced rotational alignment in Ar-NO scattering. *J. Chem. Phys.* **2001**, *115*, 6277–6280.
- (75) Wade, E. A.; Lorenz, K. T.; Chandler, D. W.; Barr, J. W.; Barnes, G. L.; Cline, J. I.

Ion imaging studies of product rotational alignment in collisions of NO ($X^2\Pi_{1/2}, j=0.5$) with Ar. *Chem. Phys.* **2004**, *301*, 261–272.

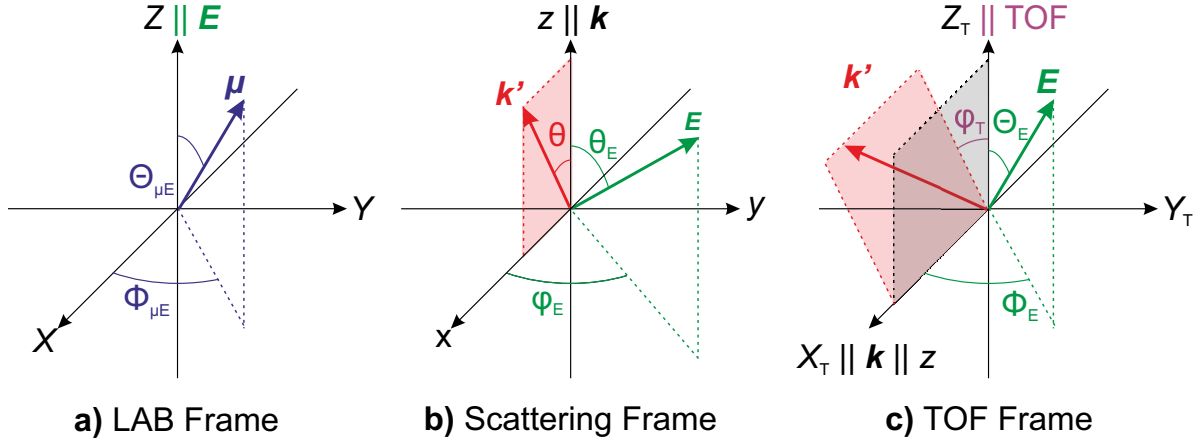


Figure 1: Definition of (a) the laboratory (LAB) frame (XYZ), (b) the scattering frame (xyz), and (c) the time-of-flight (TOF) frame ($X_T Y_T Z_T$). The direction of the dipole moment, μ , (and the parallel bond-axis, r) with respect to the direction of the static electric field in the LAB frame (a) is described by the polar and azimuthal angles, $\Theta_{\mu E}$ and $\Phi_{\mu E}$. In the scattering frame (b), the initial relative velocity, k ($= v_{Ar} - v_{NO}$), is parallel to the z -axis, k' ($= v'_{Ar} - v'_{NO}$) lies in the xz plane, and E is defined by the polar and azimuthal angles, θ_E and ϕ_E , respectively. The TOF frame (c) describes the relationship between the experimental geometry and the electric field, with ϕ_T designating the dihedral angle between the $X_T Z_T$ - and the kk' -plane.

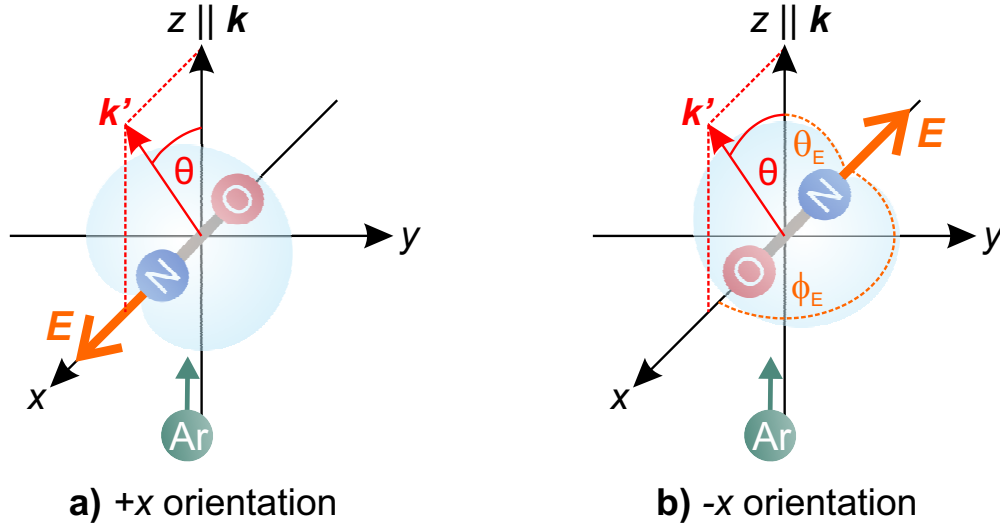


Figure 2: Schematic of the two side-on geometries in the scattering frame, in which the $+xz$ hemiplane is defined by \mathbf{k} and \mathbf{k}' . In the $+x$ configuration (a), the electric field vector, \mathbf{E} , lies along the $+x$ -axis, whilst in the $-x$ configuration (b), \mathbf{E} lies along the $-x$ -axis. The corresponding bond-axis distributions are shaded in blue and the most probable orientation, antiparallel to \mathbf{E} , is depicted by a cartoon of the molecule. The direction of the electric field is defined by the angles θ_E and ϕ_E , as indicated in (b). Note that if \mathbf{k}' were to lie in the $-x$ hemisphere, the orientation would be $-x$ in panel (a) and $+x$ in panel (b). This means that, in principle, a single experimental configuration would be sufficient to measure both geometries. In practice, this is not feasible due to the significantly lower detection efficiency in the $-x$ hemisphere.

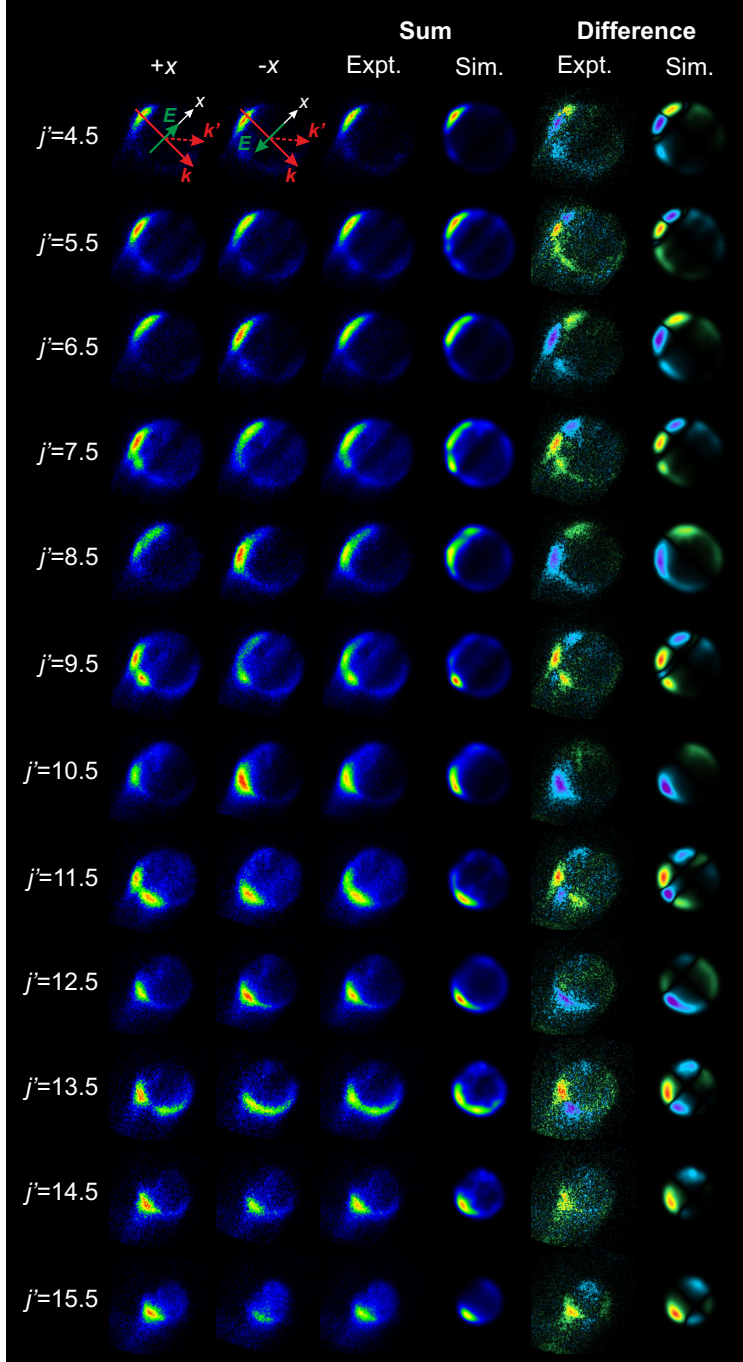


Figure 3: Experimental $+x$, $-x$, and experimental and simulated sum and difference ion images for spin-orbit conserving collisions of NO with Ar, into the final rotational state defined by $|j', \Omega' = 0.5, \epsilon' = +1, e\rangle$, for $j' = 4.5$ to 15.5. The relative intensities are conserved in the $+x$ and $-x$ images, and the field directions are indicated for $j' = 4.5$.

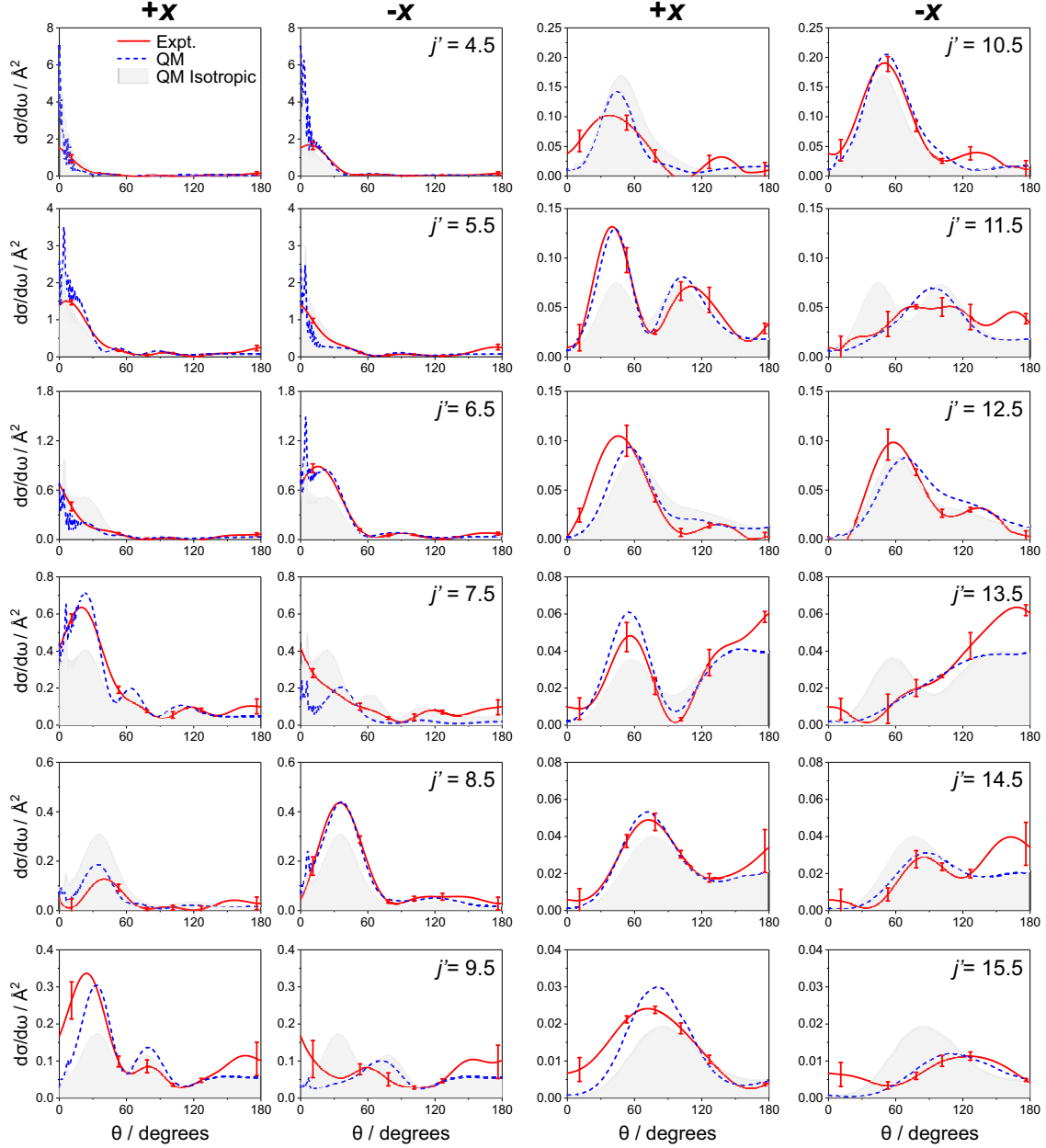


Figure 4: Experimental (red lines) and QM (blue dashed lines) x -axis oriented DCSs for the collisions of NO with Ar, into the final rotational states defined by $|j', \Omega' = 0.5, \epsilon' = +1, e\rangle$. Collisions in the $+x$ - and $-x$ -orientations are shown in panels 1,3 and 2,4, respectively. The QM (field dependent) isotropic DCS is shaded in grey. Error bars are propagated from the errors in the $R_q^{(k)}(\theta)$ moments extracted from the images in Figure 3. QM data have been averaged over a Gaussian distribution of collision energies with a FWHM of 35 cm^{-1} .

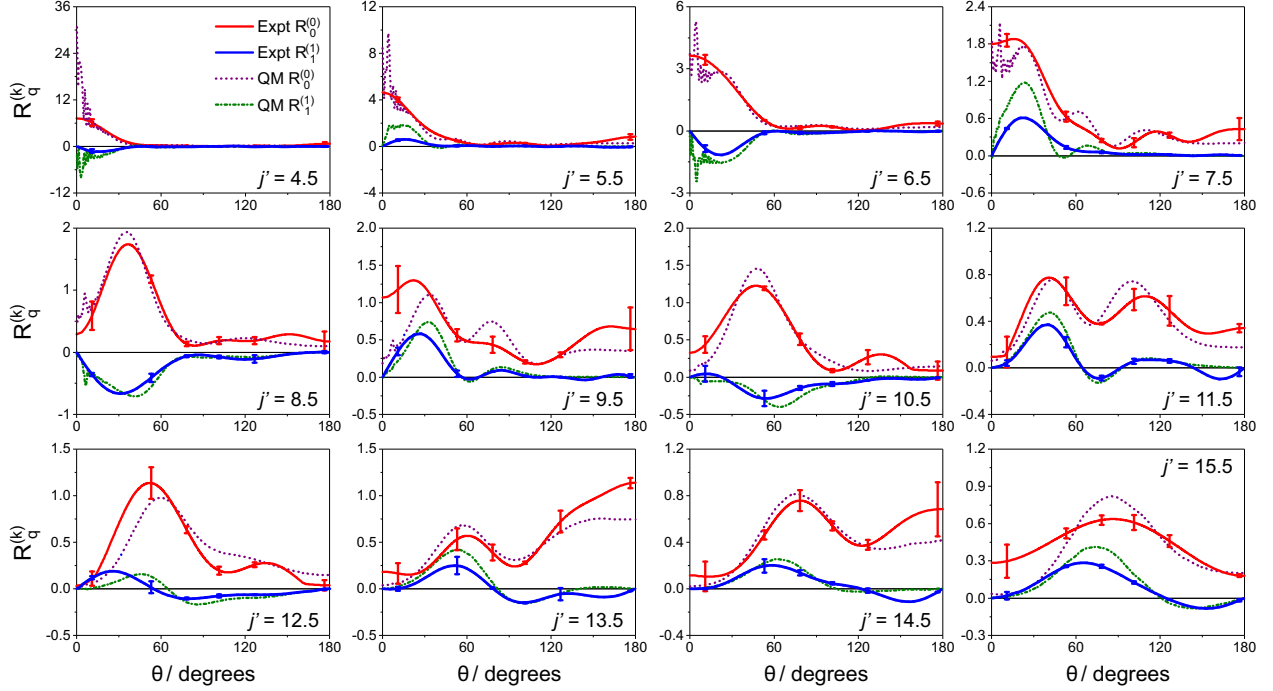


Figure 5: Experimental and QM r -PDDCSs for the collisions of NO with Ar, into the final rotational states defined by $|j', \Omega' = 0.5, \epsilon' = +1, e\rangle$. The experimental $R_0^{(0)}(\theta)$ and $R_1^{(1)}(\theta)$ moments are shown by red and blue lines, respectively. The error bars were calculated as the standard deviation of analysing the slow and fast sides of the experimental ion image as well as the whole image. The QM $R_0^{(0)}(\theta)$ and $R_1^{(1)}(\theta)$ moments are shown by purple (dotted) and green (dashed-dotted) lines, respectively. The QM data has been averaged over a Gaussian distribution of collision energies with a FWHM of 35 cm^{-1} .

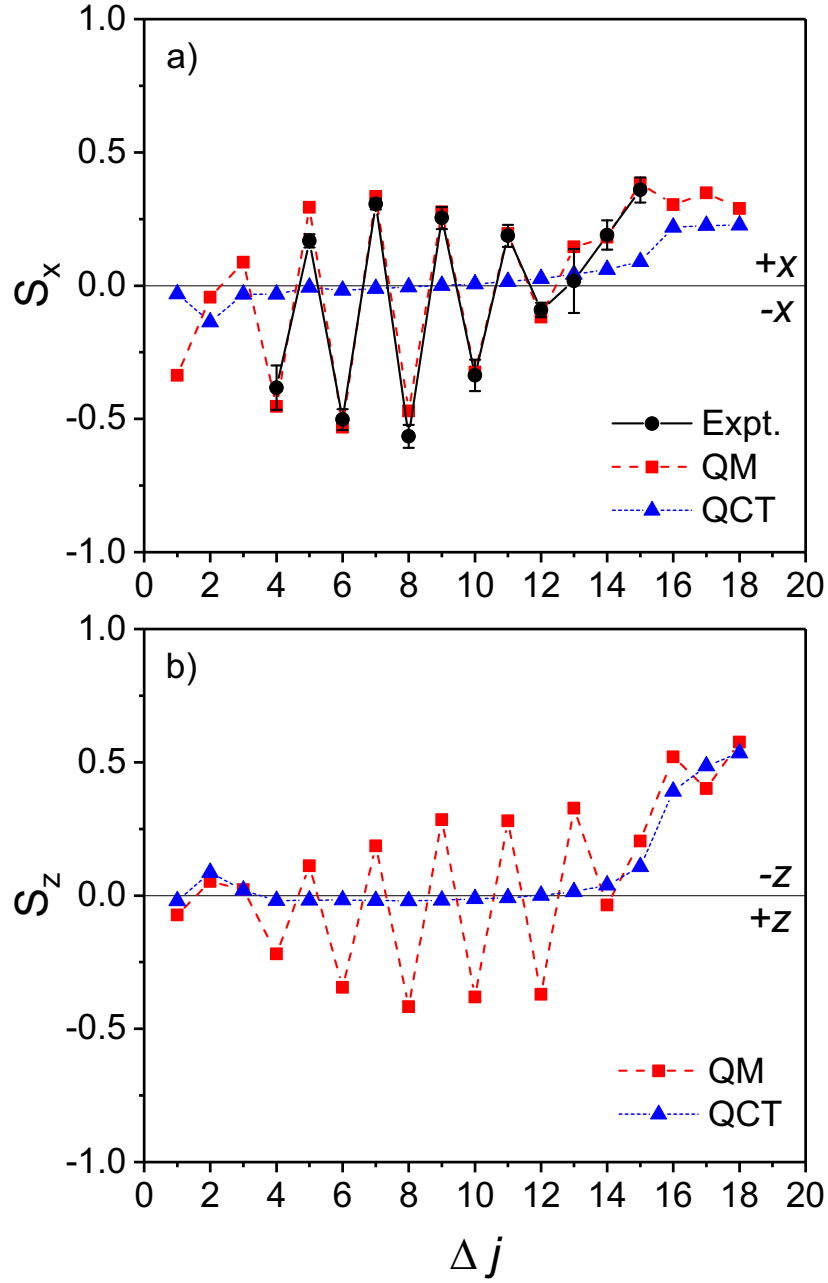


Figure 6: (a) x -axis integral asymmetry, S_x , for the spin-orbit conserving collisions of NO with Ar into the final e Λ -doublet. Experimental, QM and QCT data are shown by black lines (with circles), red dashed lines (with squares), and dotted blue lines (with triangles), respectively. Errors are propagated from the errors in the $R_q^{(k)}(\theta)$ moments extracted from the images in Figure 3. For comparison, the z -axis (end-on) QM and QCT calculated steric asymmetries, S_z , are shown in (b).¹³

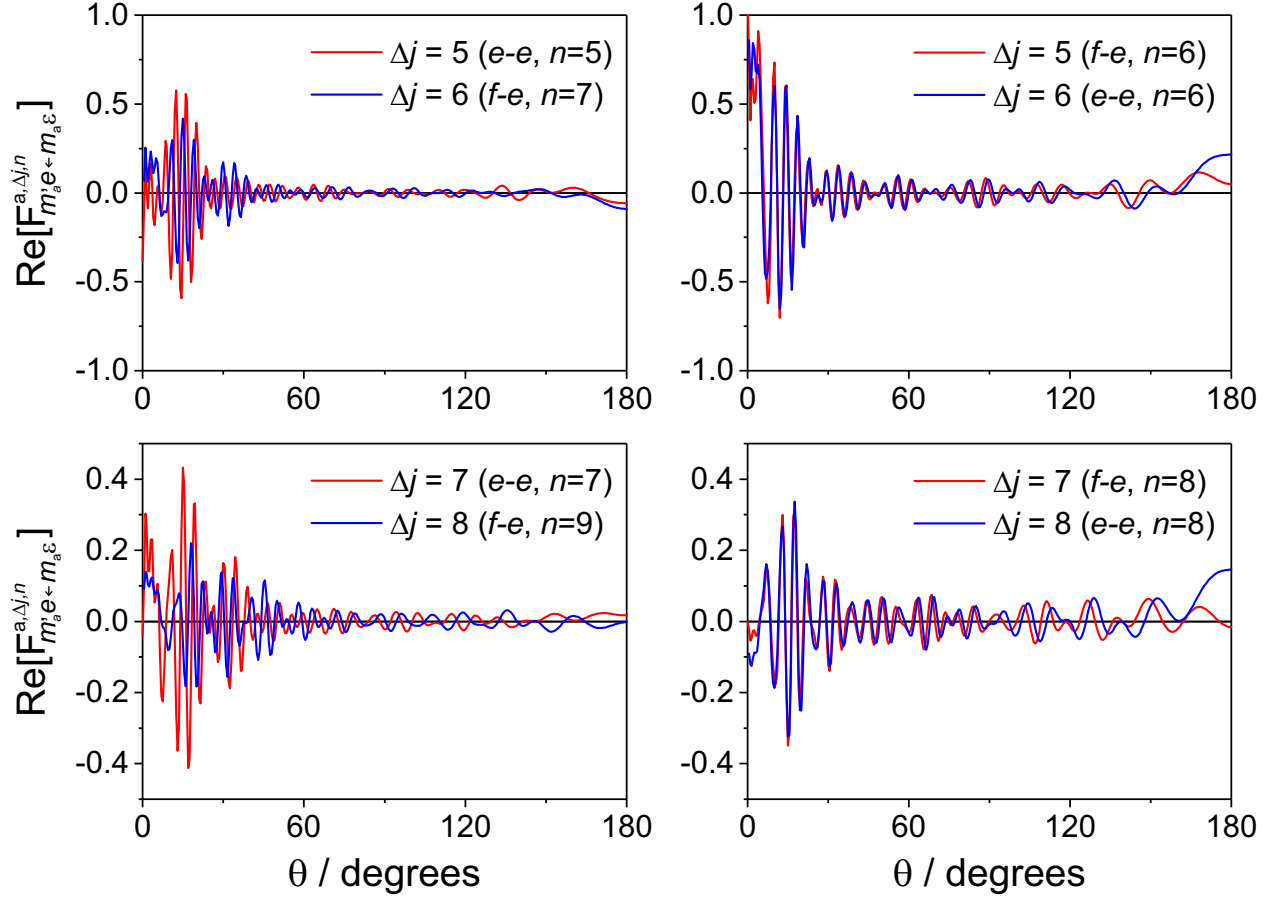


Figure 7: Apse frame field-free scattering amplitudes, $F_{m'e' \leftarrow m\epsilon}^{a, \Delta j, n}$, for $\Delta j = 5, \Delta j + 1 = 6$ (top) and $\Delta j = 7, \Delta j + 1 = 8$ (bottom), for the $\Delta m_a = 0$ transition. States with Δj and $\Delta j + 1$ are shown by red and blue lines, respectively. The left panels show the case where $n_{\Delta j} \neq n_{\Delta j+1}$, and the right panels the case where $n_{\Delta j} = n_{\Delta j+1}$, where n is calculated according to eq 40. Only the real part of the scattering amplitude is shown here, but the same trend is observed in the imaginary part.

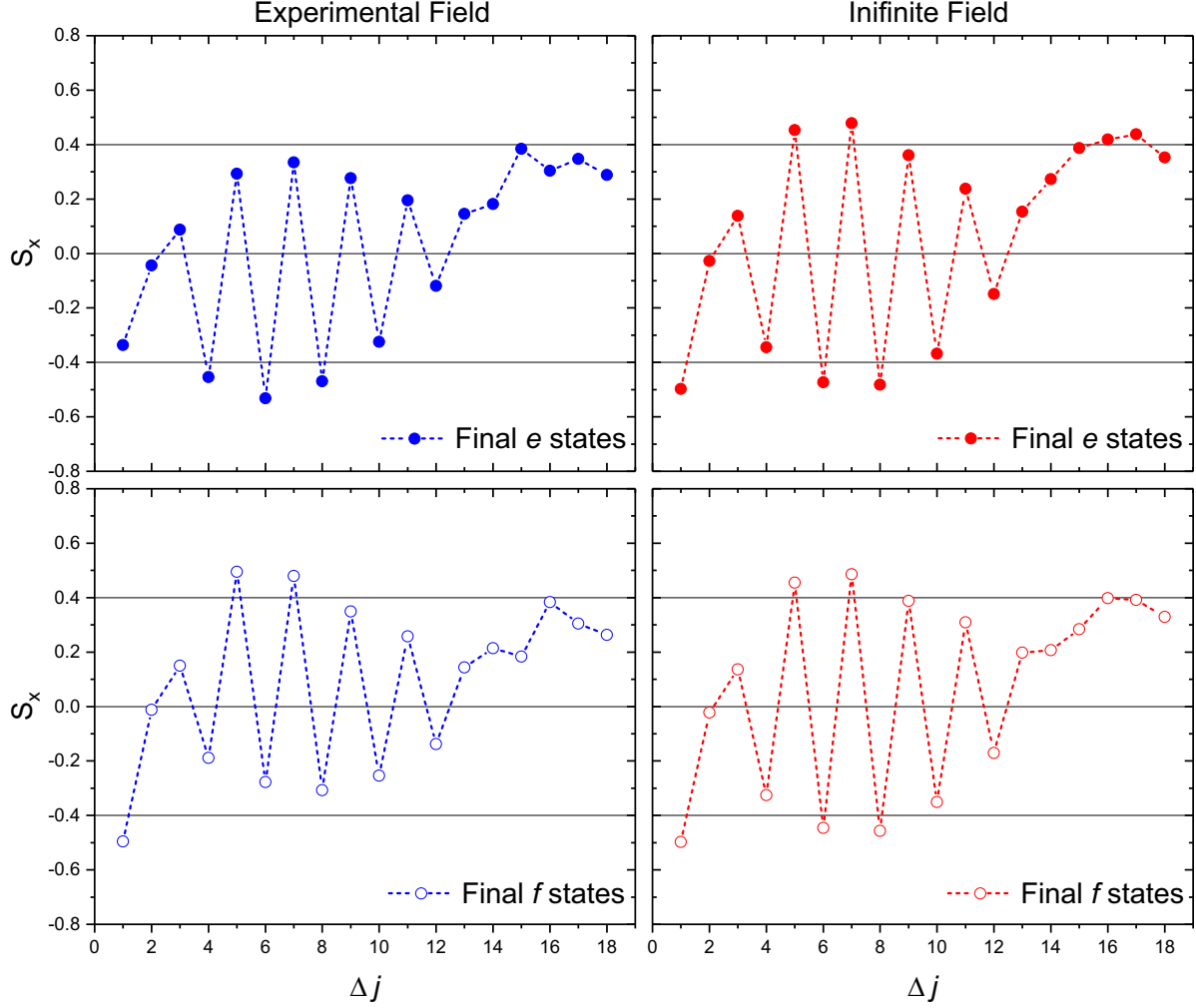
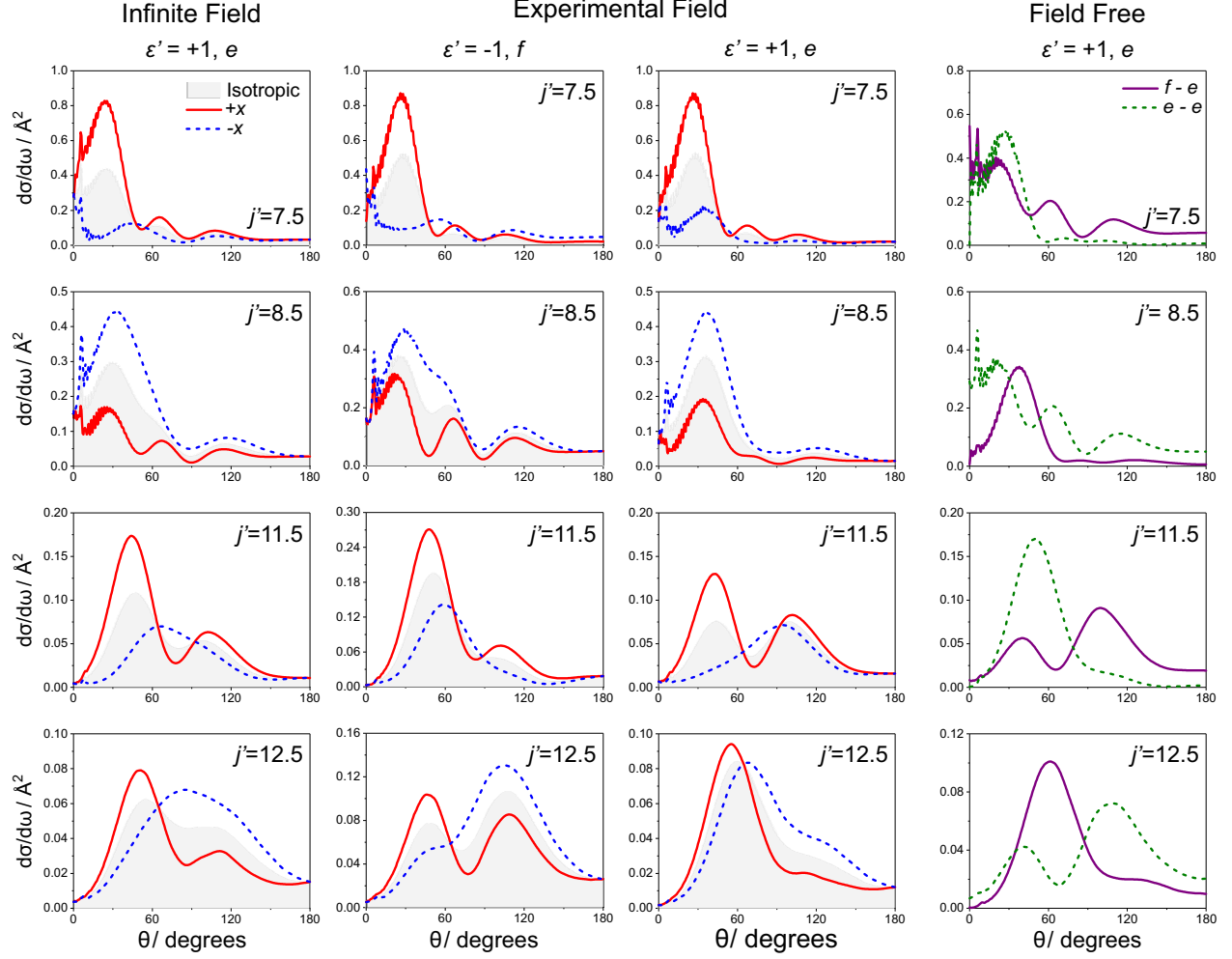


Figure 8: QM x -axis oriented integral steric asymmetries (ISA) as a function of Δj at the experimental field strength (left) and at infinite field (right). The top row represents transitions to the e final states, whilst the bottom row represents transitions into the f final Λ -doublet. Note that the ISA at infinite field is roughly symmetric around zero for both manifolds, but is shifted towards negative values at the experimental field for the final e Λ -doublet (top), and towards positive values for the final f Λ -doublet (bottom). The horizontal lines are included as a guide for the eye.



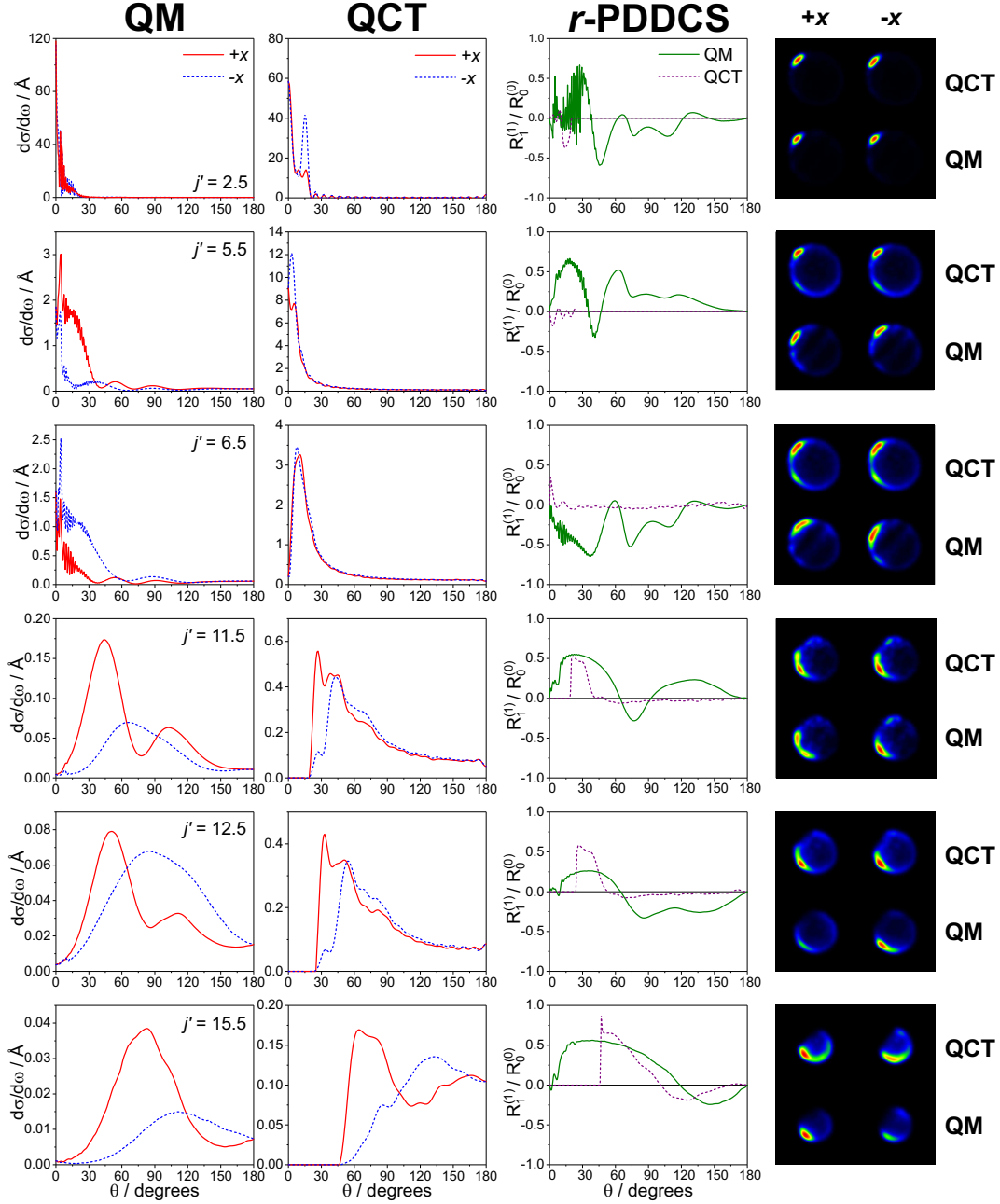


Figure 10: Comparison of QM (column 1) and QCT (column 2) bond orientation resolved DCSs for selected $|j', \Omega' = 0.5, \epsilon' = +1, e\rangle \leftarrow |j = 0.5, \Omega = 0.5, E = \infty\rangle$ transitions of NO scattering with Ar at infinite field: the $+x$ - and $-x$ -orientations are shown by red and blue (dashed) lines, respectively. The QM and QCT renormalised $R_1^{(1)}(\theta)$ moments are shown in column 3, by green and purple (dashed) lines, respectively. QCT (top) and QM (bottom) ion image simulations are shown in column 4 for the $+x$ - (left) and $-x$ -orientations (right).

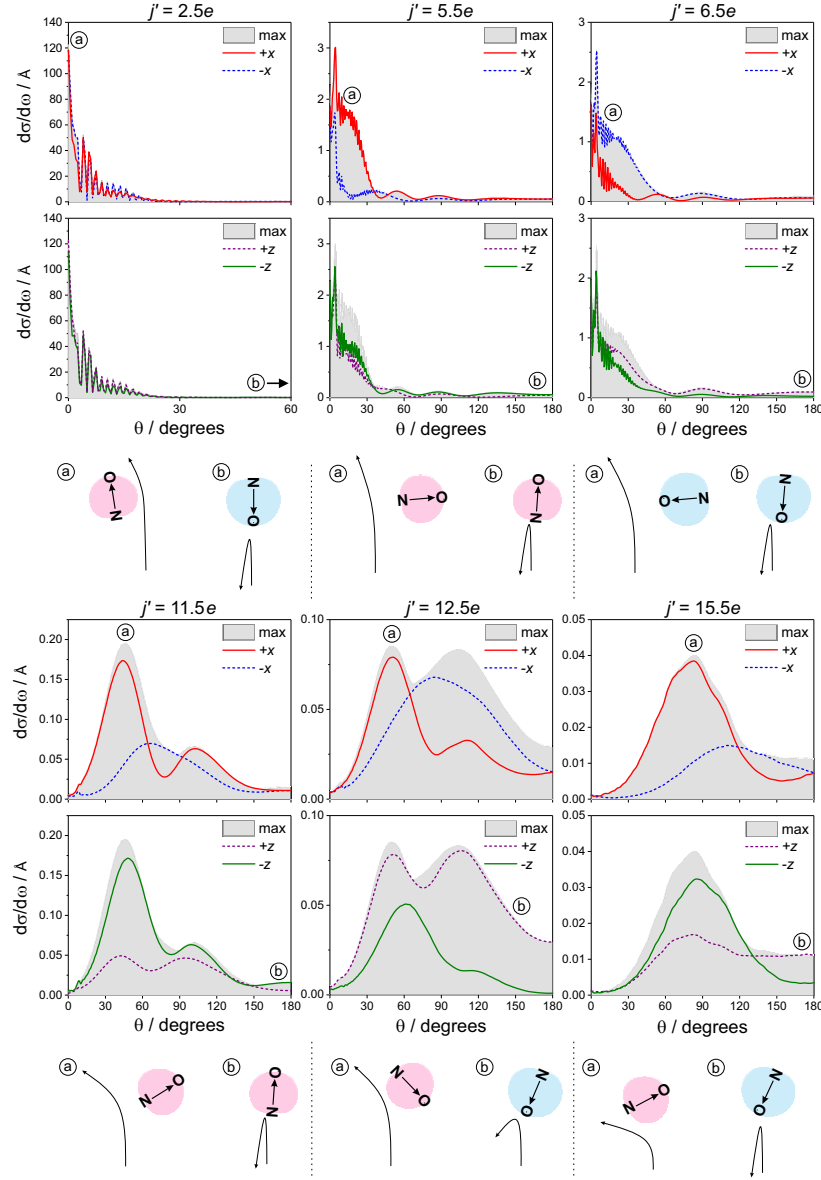


Figure 11: Infinite field maximised CC QM DCSs (grey shading) compared to $\pm x$ - and $\pm z$ -DCSs, respectively, for several final rotational states. The $+x$, $-x$, $+z$ (O) and $-z$ (N) DCSs are shown by red, blue (dashed), purple (dashed), and green lines, respectively. For $j = 2.5e$, scattering angles are shown only up to 60° , beyond which the DCS is essentially zero. The mechanistic cartoons of the preferred orientation are shown below the DCSs for (a) forwards scattering (*i.e.* $\theta < 90^\circ$), and (b) backwards scattering (*i.e.* $\theta > 90^\circ$). The shaded region shows the distribution of the bond-axis orientation, whilst the arrow shows the most probable orientation. The distributions are shaded pink and blue for repulsive collisions with the N-end/side and with the O-end/side, respectively.

Graphical TOC Entry

